ExoMars Flush Air Data System: Entry Simulation and Atmospheric Reconstruction Method

Bart Van Hove*, Özgür Karatekin†,
Royal Observatory of Belgium, 1180 Brussels, Belgium

Thorn Schleutker‡, and Ali Gülhan§
DLR, German Aerospace Center, 51147 Cologne, Germany

Flight data recorded during atmospheric entry with forebody pressure instrumentation, referred to as a Flush Air Data System (FADS), provide valuable measurements for the reconstruction of the trajectory and in-situ atmospheric conditions. We present a method to reconstruct the angle of attack, sideslip angle, and atmospheric density, pressure, and temperature in support of the post-flight analysis for the ExoMars Entry, Descent, and Landing Demonstrator Module, named Schiaparelli. Numerical predictions of the forebody surface pressure distribution, required as input to the FADS reconstruction, were developed in a companion paper. Here, we demonstrate the FADS method in a hypersonic wind tunnel at Mach 5 to 7, and study theoretical FADS reconstruction performance along a simulated EDM entry trajectory. The main error sources identified are unobserved winds and measurement bias errors, the latter are exacerbated by the limited number of pressure ports on the EDM.

Nomenclature

α = angle of attack (°)

α_T = total angle of attack (°)

β = sideslip angle (°)

$C_{p,i}$ = pressure coefficient at port i (–)

---

* Assistant Researcher, Department of Reference Systems and Planetology.
† Senior Researcher, Department of Reference Systems and Planetology, co-PI of ExoMars 2016 AMELIA group.
‡ Research Scientist, Supersonic and Hypersonic Technology Department, Institute of Aerodynamics and Flow Technology, Linder Höhe.
§ Head of Department and PI of the ExoMars 2016 instrumentation COMARS+, Supersonic and Hypersonic Technology Department, Institute of Aerodynamics and Flow Technology, Linder Höhe.

γ = heat capacity ratio (–)

g = gravitational acceleration (m/s^2)

M_∞ = Mach number (–)

m = molecular weight (kg/mol)

ϕ_T = total clock angle (°)

p_{BC} = atmospheric pressure boundary (Pa)

p_i = surface pressure at port i (Pa)

p_∞ = atmospheric pressure (Pa)

$P_{S,th}$ = theoretical stagnation pressure (Pa)

ρ_∞ = atmospheric density (kg/m^3)

r = radial distance from planet center (m)

r_{BC} = radial distance of p_{BC} boundary (m)

R = gas constant (J/mol/K)

σ = Gaussian standard deviation

θ = forebody port angle (°)

T_∞ = atmospheric temperature (K)

V_∞ = atmosphere relative velocity (m/s)

Acronyms and Initialisms

CFD = computational fluid dynamics

CG = center of gravity

DLR = German Aerospace Center

EDL = Entry, Descent, and Landing

EDM = EDL Demonstrator Module

FADS = Flush Air Data System

H2K = wind tunnel facility at DLR

IMU = Inertial Measurement Unit

MCD = Mars Climate Database

MSL = Mars Science Laboratory

NEQ = non-equilibrium

RANS = Reynolds-averaged Navier-Stokes

RSS = root-sum-squared

WT = wind tunnel

I. Introduction

The first landing on Mars was in 1971 by the Soviet Union's Mars 3 mission [1],[2] which briefly transmitted data back from the surface of Mars. Since then, only eight rovers and platforms have successfully performed Entry, Descent, and Landing (EDL) on Mars [3]–[9]. One of the most recent EDL missions was ExoMars in October 2016 by the European Space Agency (ESA), in collaboration with the Russian Space Agency (ROSCOSMOS). The ExoMars 2016 mission included an EDL demonstrator module (EDM) named Schiaparelli [10],[11]. Its main objective was to demonstrate European EDL technologies by landing on Mars and serve as precursor mission to an ExoMars 2020 rover. The EDM performed successful atmospheric entry, however a navigation error after parachute deployment resulted in a crash landing [12]. Fortunately, the EDM recorded and transmitted essential flight data during entry, which included navigation estimates as well as heat shield pressure and temperature data. The 2016 ExoMars EDM and the 2012 Mars Science Laboratory (MSL) [13],[14] are the only recent Mars entry vehicles equipped with an instrumented heat shield, next will be the NASA Mars 2020 mission [15]. Forebody pressure instrumentation, referred to here as a Flush Air Data System (FADS), provides valuable measurements for the validation of engineering models and the reconstruction of in-situ atmospheric conditions along the trajectory.

The design of EDL missions requires accurate models of aerodynamics, aerothermodynamics, and the atmosphere to design the heat shield, aeroshell geometry, and trajectory for robust performance over a wide range of flight conditions. Engineering models for this purpose are based on physics and experimental data, mainly from ground testing such as wind tunnels (WT) and computational fluid dynamics (CFD). Continued validation of these models is crucial for the design of future EDL technologies, e.g. supersonic retro-propulsion, inflatable heat shields, and improved guidance [16]–[19]. Key challenges for flight validation are the limited number of Mars EDL missions, and the need for adequate flight instrumentation. Historically, EDL flight data have included acceleration and angular rates recorded by an inertial measurement unit (IMU) [7]. The IMU rates are numerically integrated

over time to reconstruct an inertial (planet-relative) trajectory, often assuming zero winds in the identification of atmosphere relative velocity and flow angles. Atmospheric density can be reconstructed by combining IMU acceleration data with assumed aerodynamic force coefficients [20]. Pressure and temperature are then derived from density by virtue of hydrostatic equilibrium and the ideal gas law. The main disadvantage of IMU flight data is that the atmospheric density is reconstructed using aerodynamic models. Consequently, the models cannot be validated and aerodynamic uncertainties are propagated directly to the atmospheric reconstruction. Aerodynamic uncertainty is significant, e.g. the 3-σ uncertainty on axial force coefficients can be as high as 5–10% [21]. Beyond engineering validation, this also affects the scientific study of atmospheric reconstructions based on EDL data. Flight data from every Mars EDL mission have been used to advance our understanding of the atmosphere on Mars [22]–[28]. While remote atmospheric observations from Mars orbit are now routine [29], the advantages of flight data are that the reconstructed density, pressure, and temperature conditions are in-situ and have good spatial resolution, as well as covering large altitude ranges of up to 0–130 km [30]. These characteristics are important to resolve atmospheric phenomena such as thermal tides, gravity waves, and cloud formation.

The key advantage of FADS flight instrumentation is that atmospheric conditions and flow angles are reconstructed with far less dependence on aerodynamic models. By combining FADS pressure data with a model of the forebody surface pressure distribution, and the relative velocity commonly given by IMU, the atmospheric density and flow angles can be derived. Because the pressure model is based on CFD predictions, similar to aerodynamic models, there is potential for models to contain similar errors. However, the FADS pressure model is only used at forebody locations where surface pressures are measured, as opposed to aerodynamic modeling which requires accurate pressures on the whole vehicle surface. This reduces uncertainty compared to the IMU approach, in particular for density which is mainly based on the stagnation pressure and shock wave pressure ratio. By comparison, the flow angle reconstruction is more sensitive to pressure differences across the heat shield, hence more dependent on the available number of FADS ports and local errors in the CFD pressure model. If the FADS is able to reconstruct flow angles with very high accuracy, on the order of 0.1° [9], it is also possible to reconstruct winds by combining flow angles from FADS with inertial attitude from IMU. This is more feasible in supersonic flight, where the wind speed and flight velocity are closer than in hypersonic flight [31]. For MSL, the winds have been reconstructed in the supersonic regime using 7 pressure ports [9]. Here, we do not attempt wind reconstruction as the EDM has only 4 pressure ports, and our results show this is not sufficient for this purpose.

The FADS instrumentation on MSL has been studied extensively in the literature, where pressure data were used to reconstruct the flow angles, aerodynamic coefficients, and atmospheric conditions during MSL's entry [9],[31]–[35].

Compared to MSL, the FADS on ExoMars EDM differs in some important ways. Firstly, only four ports are available on the front heat shield. Secondly, the ports are in other locations relative to MSL due to the different flight conditions of these entry vehicles. MSL flew a lifting trajectory at negative angles of attack between –15° and –20°, while the EDM performed ballistic entry at low angles of attack. Ballistic entry is more common on Mars, and in fact the EDM aeroshell and trajectory are similar to those of previous EDL missions such as Phoenix [21], the Mars Exploration Rovers [8], and InSight arriving on Mars in 2018 [36]. This makes the present work relevant to ballistic Mars entry vehicles in general. The main contribution of this paper is a detailed description of FADS methodology that will be used in the ExoMars EDM post-flight analysis, including the CFD pressure model for the EDM developed in companion paper [37]. We demonstrate the FADS method in a hypersonic wind tunnel, using a similar CFD pressure model developed for wind tunnel conditions by [37], which also describes the experimental setup. We verify the correct implementation of the FADS method, and evaluate its accuracy within experimental uncertainties. Finally, we study the theoretical FADS performance along a simulated EDM entry trajectory, including uncertainties from the FADS data, CFD pressure model, and assuming zero winds. We conclude by evaluating the FADS performance and making recommendations for the EDM post-light analysis.

II. Flush Air Data System

A. ExoMars EDM entry vehicle

The ExoMars EDL Demonstrator Module is a ballistic entry vehicle, meaning the total angle of attack is close to zero. The EDM aeroshell is illustrated in Fig. 1a and consists of a blunted sphere-cone with 70° half-angle and 2.4 m outside diameter, which tapers off at a half-angle of 47°. This geometry is dynamically stable in the hypersonic flight regime, but becomes unstable at lower speeds. A parachute is deployed near 10 km at about Mach 2, after which the front heat shield is jettisoned. This prevents heat from soaking into the EDM during the descent phase, reduces mass, and permits radar altimeters behind the heat shield to operate. The parachute descent was to be followed by retro-boosting and landing on a crushable structure. During the actual flight, the on-board navigation incurred an attitude error due to gyroscope saturation, during parachute deployment. This led to the premature ignition of the retro-boosters at a few kilometers above ground, after which radio contact was lost and the EDM crash landed [12]. However, the EDM transmitted IMU and FADS data during flight, excluding the radio blackout period between about 70 and 30 km. While flight data are not processed in this paper, the simulated FADS study in Section IV will focus on the trajectory region where actual data are available, below 30 km when the vehicle decelerated through Mach 14.

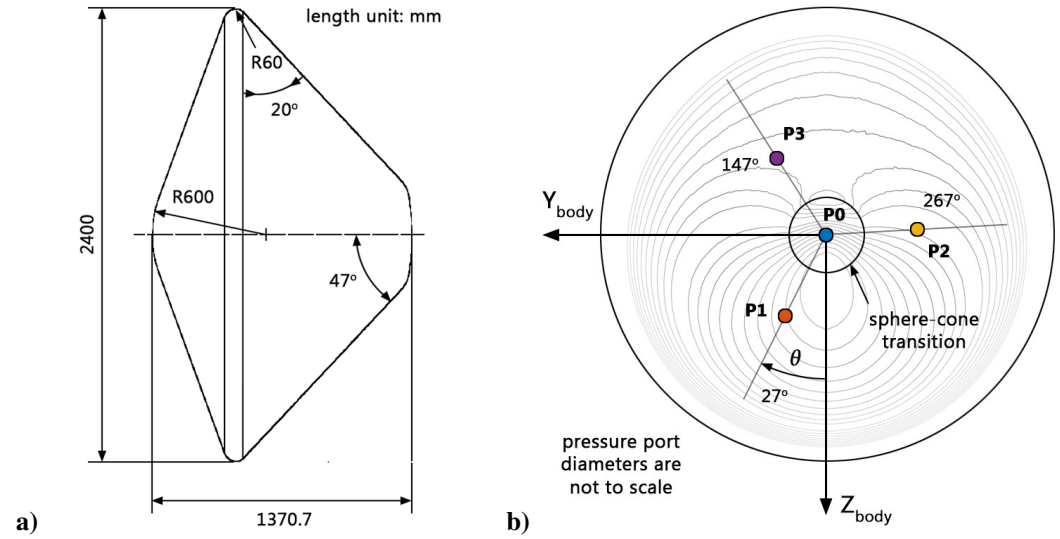

Fig. 1 EDM vehicle a) side and b) frontal view with FADS ports, with CFD pressure contours.

The FADS measured forebody pressures during the hypersonic–supersonic atmospheric entry phase, until heat shield jettison. The heat shield is made of an ablative material called Norcoat-Liège [12]. Four pressure ports are shown in Fig. 1b in the EDM body frame, they are connected to Kulite pressure transducers with a measurement range of 25 kPa, on the back of the heat shield. Port angles θ in Fig. 1 indicate the angular locations of pressure ports. The off-center ports P1, P2, and P3 are separated by 120° at a radial distance of 0.480 m from the centerline [12]. Their radial locations about halfway between the centerline and shoulder are convenient for CFD modeling, which is more challenging near the sphere-cone transition and shoulder [37]. The angular locations are intended to situate port P1 near the aerodynamic trim plane of the EDM, with the center of gravity (CG) being near the positive Z-axis in the body frame (see Section IV.A). Fig. 2 gives definitions for positive angle of attack α, sideslip angle β, total angle of attack α_T, and total clock angle ϕ_T. Either pair of (α, β) or (α_T, ϕ_T) is sufficient to express wind-relative attitude, i.e. the direction of atmosphere relative velocity V_∞ in the body frame. While the definitions of α, β, and α_T are standard, that of ϕ_T is not. ϕ_T increases clockwise from the body z-axis looking aft, and varies in the range of ±180°.

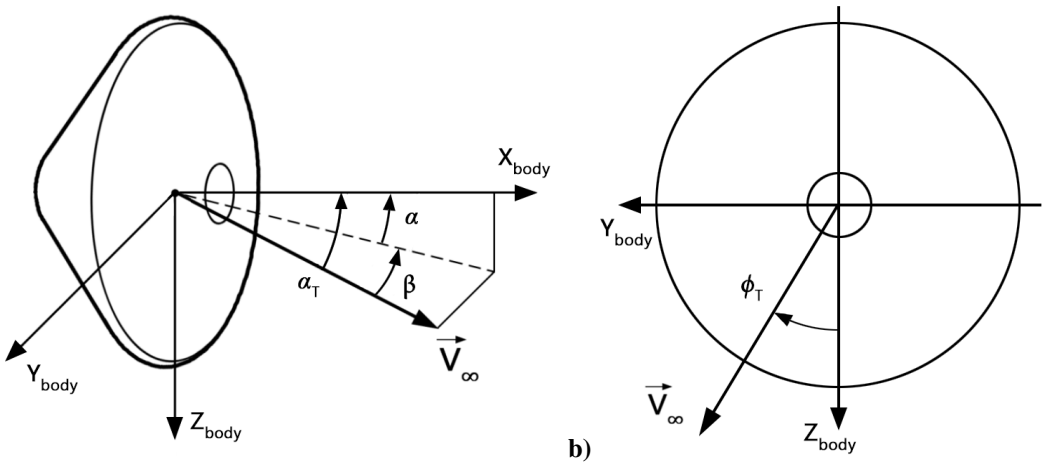

Fig. 2 Body frame at positive angle of attack, sideslip angle, total angle of attack, and total clock angle.

B. FADS reconstruction method

Given a model of the forebody pressure distribution, the FADS method searches parameters that maximize the least-squares agreement between CFD pressure model and FADS measurements. The method given here solves for angle of attack, sideslip angle, and atmospheric density. Pressure and temperature are derived from reconstructed density using relations from hydrostatic equilibrium and the ideal gas law. In principle, the Mach number can be estimated from the measured pressure distribution as well. However, the effect of the Mach number on the distribution is secondary to that of density and the flow angles. This is known from hypersonic theory, where the surface pressure becomes independent of the Mach number for very fast isentropic flows [38]. Instead, we derive the Mach number from V_∞ and speed of sound based on FADS reconstructed temperature, as was done with MSL [9]. Atmosphere relative velocity, as well as the altitude, are provided by IMU as these are not observable by FADS. Note that V_∞ from the IMU assumes no winds: errors due to winds will be quantified in the uncertainty analysis of Section IV.

Surface pressure p_i at forebody location i can be normalized into a non-dimensional pressure coefficient

$$C_{p,i} = \frac{p_i - p_\infty}{\frac{1}{2}\rho_\infty V_\infty^2} \tag{1}$$

with atmospheric pressure p_∞ and atmospheric density ρ_∞. In the denominator we have the free-stream dynamic pressure. To reconstruct ρ_∞ using Eq. (1), the pressure coefficient $C_{p,i}$ must be provided by a pressure model. When multiple FADS ports at locations i are available, a system of Eq. (1) is solved as least-squares problem to match the CFD pressure model with every p_i. In hypersonic flight, the atmospheric pressure in Eq. (1) is not very significant, as p_∞ is negligible compared to p_i. However, p_∞ becomes relevant in the supersonic regime and is always included in

Eq. (1). Because p_∞ is derived from the reconstructed density, an iterative process is required. The resulting FADS method is shown in Fig. 3, where p_i measurements are normalized into $C_{p,i}$ using density estimates from the solver and V_∞ from IMU. The parameters α, β, and ρ_∞ are highlighted in red because they are solved by the least-squares method, which minimizes the residuals between C_p from FADS measurements and CFD pressure model. It converges when the RSS of relative residuals goes below 10^{-12}.

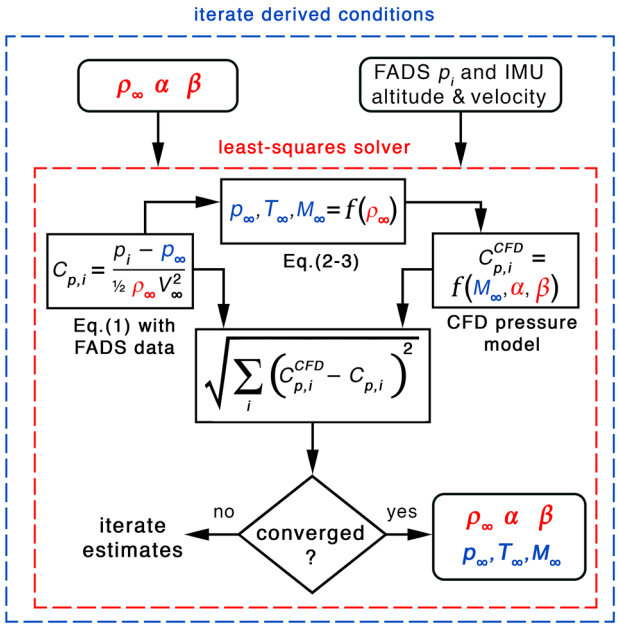

Fig. 3 FADS method: least-squares solver for density and attitude (red), global iteration of derived conditions (blue).

In several steps, the Mach number is derived from p_∞ and used to query the CFD pressure model in the least-squares solver. When the solver converges, its density estimate is used to update the Mach number. The global process is repeated until Mach number changes are less than 0.01 on the whole trajectory. Initial values are $p_\infty = 0$ and M_∞ based on constant speed of sound 220 m/s. Convergence is typically reached after 2–4 iterations. The derivation of p_∞ from density is based on the hydrostatic equilibrium relation in Eq. (2), in which ρ_∞ is integrated over altitude using a numerical trapezoid method. The boundary condition p_{BC} is provided by an atmospheric model, typically at some high altitude:

$$p_\infty = p_{BC} - \int_{r_{BC}}^{r} g(r)\rho_\infty(r)\,dr \tag{2}$$

with radial distance r from the planet center and the gravitational acceleration $g(r)$ defined positive down, which is computed with an ellipsoid gravity model. Once p_∞ has been derived with respect to altitude, the atmospheric temperature T_∞ is derived by the ideal gas law

$$T_\infty = \frac{p_\infty}{\rho_\infty}\frac{m}{R} \tag{3}$$

with mean molecular weight m of approximately 0.044 kg/mol on Mars, and gas constant R in J/mol/K. The Mach number is calculated from relative velocity and temperature as $M_\infty = V_\infty / \sqrt{\gamma R T_\infty}$ with heat capacity ratio γ of about 1.3. In the EDM flight analysis of Section IV, the properties m and γ depend on altitude and are given by an atmospheric model. In the wind tunnel tests of Section III, the free-stream pressure and Mach number are assumed known and the global iteration (blue in Fig. 3) is disabled.

III. FADS validation in H2K wind tunnel

The FADS method from Section II is demonstrated in the H2K cold gas hypersonic wind tunnel (WT) facility at DLR. The wind tunnel demonstration allows to evaluate the global performance of the FADS method, and partially validate the CFD model at flight conditions. Flow angles and free-stream density are reconstructed from pressure data, recorded on a 1:16 scaled model of the ExoMars EDM. [37] provides more details on the experimental setup and wind tunnel facility, only essential information is given here. The WT model of the EDM is shown in Fig. 4 and instrumented with 9 pressure ports, leading to a single pressure transducer inside the model and calibrated to 0.1% (3-σ). During an experiment, the surface pressures are recorded sequentially per port. The FADS ports on the WT model are not clocked at 120° as on the EDM, but more numerous in total and more densely clustered in the pitch plane (P1–P4), as well as on one half of the forebody (P5–P7). As the wind tunnel does not reproduce the EDM flight conditions exactly (e.g. no, air gas instead of CO_2), the port layout is not intended to replicate the EDM, but instead to measure the pressure distribution with high spatial resolution. This improves the accuracy of the FADS in the wind tunnel, providing experimental validation of the CFD modeling approach also used for the EDM flight conditions in Section IV. In [37], a CFD pressure model was developed for the wind tunnel conditions in particular. While the cold gas flow reducing demands on the CFD compared to flight, applying the FADS in a wind tunnel introduces some experimental uncertainties not present during entry. These include flow alignment, uniformity, and repeatability as discussed in this section.

A. Experimental setup

The wind tunnel experiments involve cold air at Mach numbers of 5.3, 6, and 7. The WT model is oriented with a sting mechanism at angles of attack up to ±9°. The sideslip angle is always zero, reducing the number of tests and exploiting the flow symmetry, as discussed below. At every Mach number, α ranges from 0° to 6° in increments of 1°, after which two more experiments are performed at +9° and –9°. The negative α tests are used in [37] to evaluate flow uniformity and alignment using the WT model itself. When comparing the $\alpha = \pm 9°$ tests, ideally the pressures at ports P4, P8 and P5, P7 should interchange, while remaining identical at P1, P6, and P9. Normalized pressure data were considered to exclude tunnel repeatability from the comparison. This flow quality test lumps together the remaining effects of flow alignment, uniformity, and blockage due to the WT model. Deviations from the perfect case just described are below 0.5%, which is used here as combined uncertainty (3-σ) due to flow quality. The sting mechanism is accurate to ±0.1° (3-σ) in terms of α and ±0.2° in terms of β. The sideslip uncertainty is higher, because the model installed on the sting has no reference surface to measure β. In the experiments, no reference values of the free-stream density are available beyond approximate values computed from measured reservoir pressure and temperature. The EDM model left no space in the test section to include a stagnation pressure probe to measure the free-stream density. This topic will be discussed in Section III.C when evaluating the FADS results.

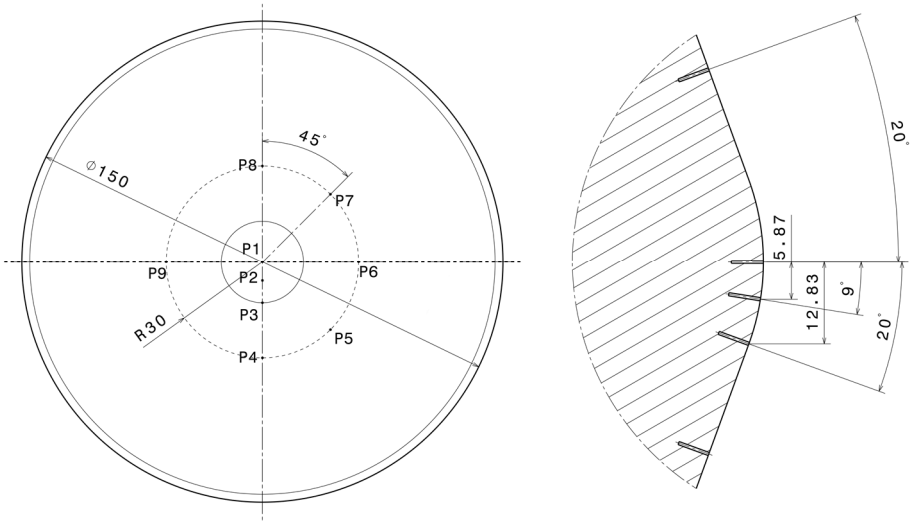

Fig. 4 WT model of scaled EDM with 9 pressure ports on the forebody from [37] (units in mm).

The 9 pressure ports on the WT model in Fig. 4 are positioned taking into account the axial symmetry of the EDM, and the vertical symmetry of the pressure distribution at angle of attack. Ports P1–P4 are in the symmetry plane, which contains the stagnation point given the zero sideslip angle. Port P2 is located at 9° from the centerline, where the

stagnation point is predicted for $\alpha = 9°$ by Newtonian impact theory [39]. Port P3 lies on the sphere-cone transition at 20°, and ports P4–P8 are spaced radially on the right half of the WT model. By comparison, the other half of the model has only port P9 without counterparts to ports P5 and P7. This reduces the number of ports, while closely spacing P4–P8 increases the angular resolution of the port layout which benefits flow angle reconstruction. The compromise is that a smaller number of ports is sensitive to left-right pressure changes due to sideslip, but it is emphasized that ports P4–P8 do provide information on β. As seen in Fig. 2, when $\beta \neq 0°$ then also the total clock angle $\phi_T \neq 0°$. In other words, the pressure distribution rotates in the body frame so a non-zero sideslip angle influences the pressure distribution at every off-center port location. The FADS reconstruction in Section III.C will confirm that the port layout performs well for both α and β angles.

B. CFD pressure model

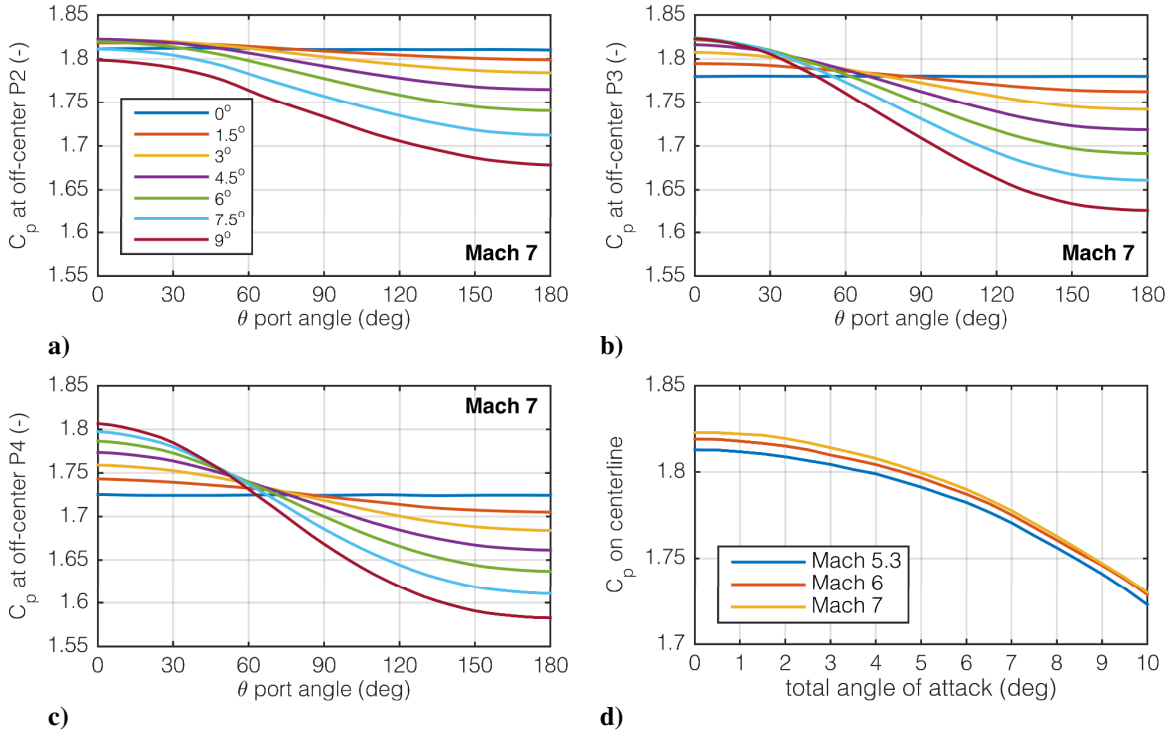

Fig. 5 CFD pressure model for WT model, a–c) off-center pressure coefficients, and d) the centerline.

The pressure distribution model, used in the FADS method, is constructed from CFD solutions for nominal wind tunnel conditions given in [37]. Reynolds-averaged Navier-Stokes (RANS) equations were solved for the wind tunnel flow, which is turbulent. CFD solutions were obtained for angles of attack from 0° to 10° in 0.5° increments,

with β zero. Notice that 10° is greater than the maximum angle of attack realized in experiments, to allow the least-squares solver in the FADS method to iterate near flow angle estimates at $\alpha \approx 9°$. Pressure coefficients as defined by Eq. (1) are extracted from the CFD solutions. C_p coefficients on the centerline describe the surface pressure at port P1 as a function of angle of attack. Away from the centerline, C_p is extracted at the radial distances of pressure ports P2, P3, and P4–P9, respectively. The off-center C_p coefficients also depend on the port angle θ (see Fig. 1) which is ranged from 0° to 180° in 22.5° increments. The pressure model is converted to (α, β) for use in the FADS method. As explained before, $\beta \neq 0°$ corresponds to a rotation of the pressure distribution, hence the pressure model is valid for any (α, β) combination even if the CFD simulations only varied the angle of attack.

Fig. 5 shows the CFD pressure model in its original form as a function of (α_T, θ), showing only some values of α_T for clarity. Fig. 5a–c shows the off-center C_p coefficients at radial distances of ports P2, P3, and P4 respectively. Notice that ports P5–P9 are at the same radial distance as port P4 so equivalent on these graphs. Fig. 5a–c shows the CFD model at Mach 7, which is similar at other Mach numbers. Fig. 5d gives the centerline C_p coefficients, which are independent of θ and plotted against α_T per Mach number. The pressure coefficients in Fig. 5 are decreasing from the windward side ($\theta <$ 90°) towards the leeward side ($\theta >$ 90°), and more so at higher total angles of attack. When α_T approaches zero, the surface pressure distribution becomes axially symmetric, i.e. independent of ϕ_T. Because the flow angles from FADS are based on the pressure differences between ports, the windward–leeward pressure reduction is related to the FADS sensitivity to attitude. Comparing the CFD pressure model at P2, P3, and P4 in Fig. 5a–c, the maximum reductions at α_T = 10° are 10.2%, 13.7%, and 15.8% respectively. In Fig. 5d, the reduction at centerline port P1 for α_T increasing from 0 to 10° is only 5.3%. This confirms our previous statement that stagnation pressure is less sensitive to attitude than off-center port locations. It is worth mentioning that Newtonian theory [39] would predict identical C_p for ports P3 and P4 at $\theta = 0°$, since the flow incidence angle on the conical forebody is identical to that on the sphere-cone transition (see Fig. 4). The CFD pressure model deviates from Newtonian theory because it considers the local expansion at the sphere-cone transition, which affects the downstream pressure.

C. FADS reconstruction with pressure data

Surface pressures measured on the WT model are shown in Fig. 6 versus angle of attack and per Mach number, with values for $\alpha = -9°$ shown at +9° to save space. Surface pressures at ports P1–P3 near the centerline (blue) are highest, as they are nearest to the stagnation point. The off-center pressures are smaller and diverge with increasing angle of attack, resulting in a larger windward-leeward difference as mentioned in Section III.B. The pressure data

in Fig. 6 have been normalized with theoretical stagnation pressure $P_{S,th}$, calculated from reservoir conditions using ideal gas equations for the nozzle expansion [37]. While the FADS method uses surface pressures in physical units, the normalization is useful in graphs to reveal pressure trends with respect to angle of attack. The normalization also shows that theoretical stagnation pressure varies between tests, e.g. the dip at α = 2° for Mach 7. Furthermore, at zero angle of attack the normalized centerline pressure is not exactly 1. This is common in wind tunnels, which is why stagnation probes are often used to estimate the free-stream density. Even without such reference values, the FADS density estimates below can still be evaluated qualitatively.

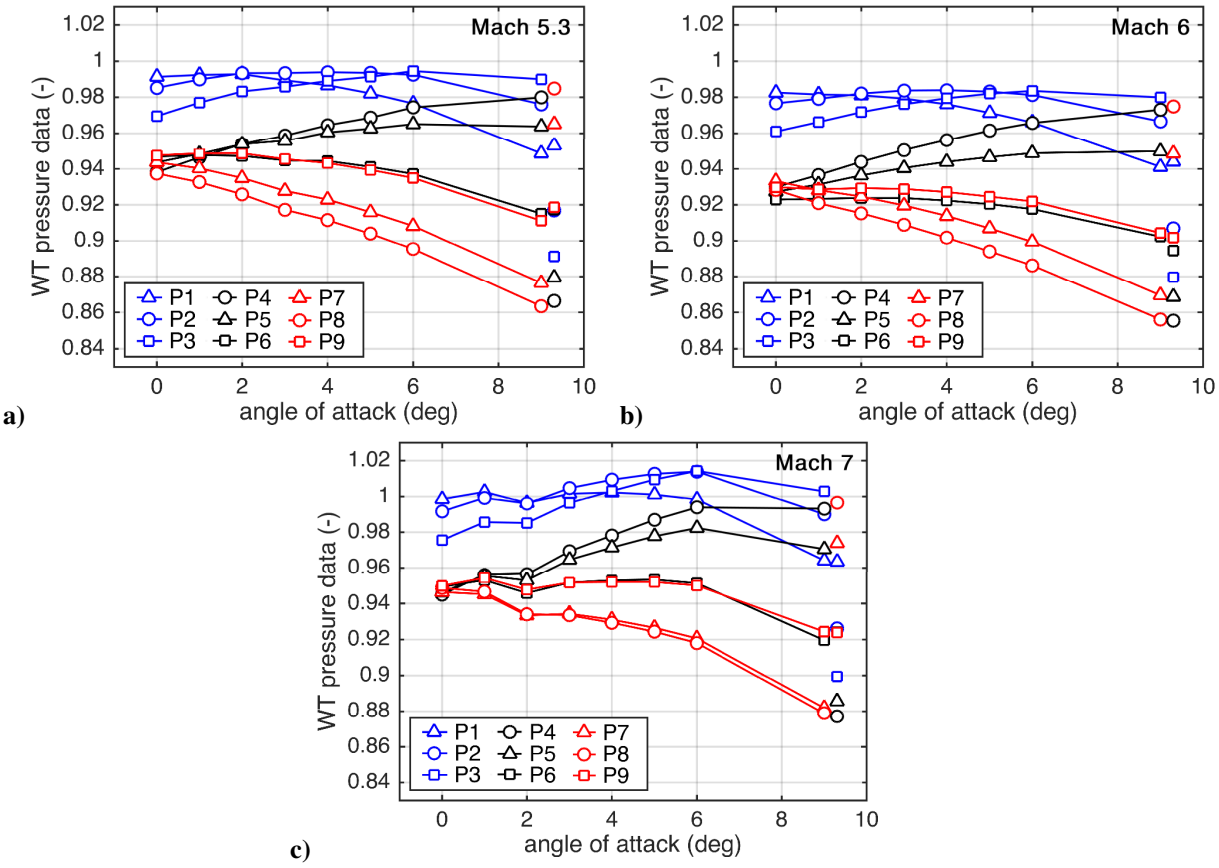

Fig. 6 Normalized pressure data from wind tunnel at Mach 5.3, 6, and 7, with α –9° at +9°.

The pressure data p_i and CFD pressure model are used in the FADS method to reconstruct flow angles and density for each wind tunnel experiment separately. The required conditions p_∞, V_∞, and the Mach number (see Fig. 3) are assumed from the nominal WT conditions given in [37]. Initial guesses α, β, and ρ_∞ for the least-squares solver are picked arbitrarily to confirm they have no effect on converged results, their errors are up to 5° on flow angles and 50% on density. Uncertainty bounds on the FADS results are calculated by Monte Carlo analysis of 1000

runs, imposing zero-mean Gaussian noise of 0.5% (3-σ) on pressure at every port. This value includes the sensor calibration of ±0.1%, and uncertainty due to flow uniformity and alignment as estimated in [37]. Because the latter have been lumped and expressed as pressures on the WT model, they are assigned here as uncorrelated pressure data errors. No uncertainty is attributed to the CFD pressure model, which then remains to be validated within experimental uncertainties.

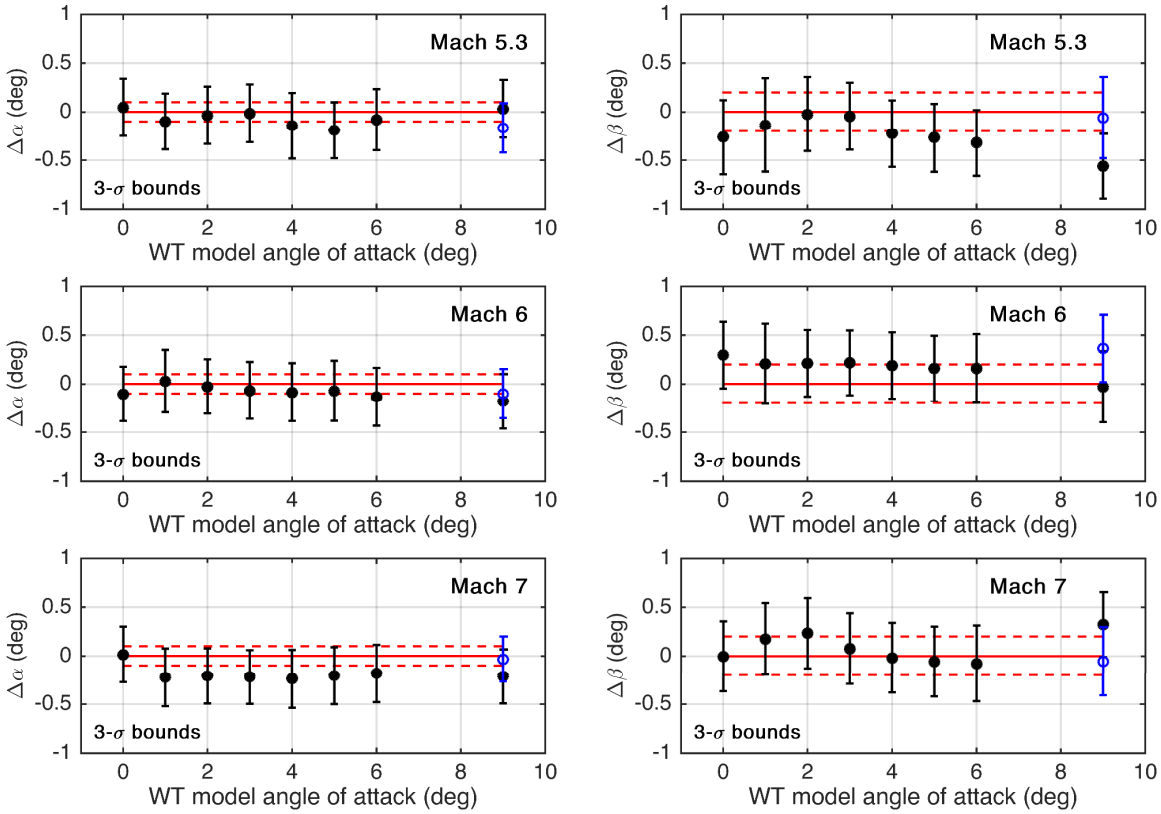

Fig. 7 FADS flow angles and Monte Carlo bounds (black) from sensor and flow quality, WT model orientation uncertainty from sting mechanism (red), α –9° at +9° (blue).

The flow angles reconstructed by FADS are plotted in Fig. 7 with respect to reference values from the sting mechanism. Uncertainty on the sting mechanism is shown by red dashed lines, and slightly larger for β. The black error bounds are from Monte Carlo and represent pressure sensor uncertainty, flow alignment and uniformity. Overall, the FADS method is accurate to about ±0.2°, with few β outliers up to 0.3° and 0.5° at Mach 5.3 and 7. The FADS accuracy for α and β is similar, as well as their Monte Carlo bounds, confirming that the port layout (see Fig. 4) is able to resolve both flow angles. Generally, the FADS flow angles and CFD pressure model are validated within experimental uncertainty. Interestingly, experiments that exhibit the largest deviations from theoretical stagnation pressure, e.g. α = 2° at Mach 7 (see Fig. 6), do not have worse flow angle reconstructions. This confirms

the secondary importance of the overall magnitude of the pressure distribution for flow angles, as opposed to for density.

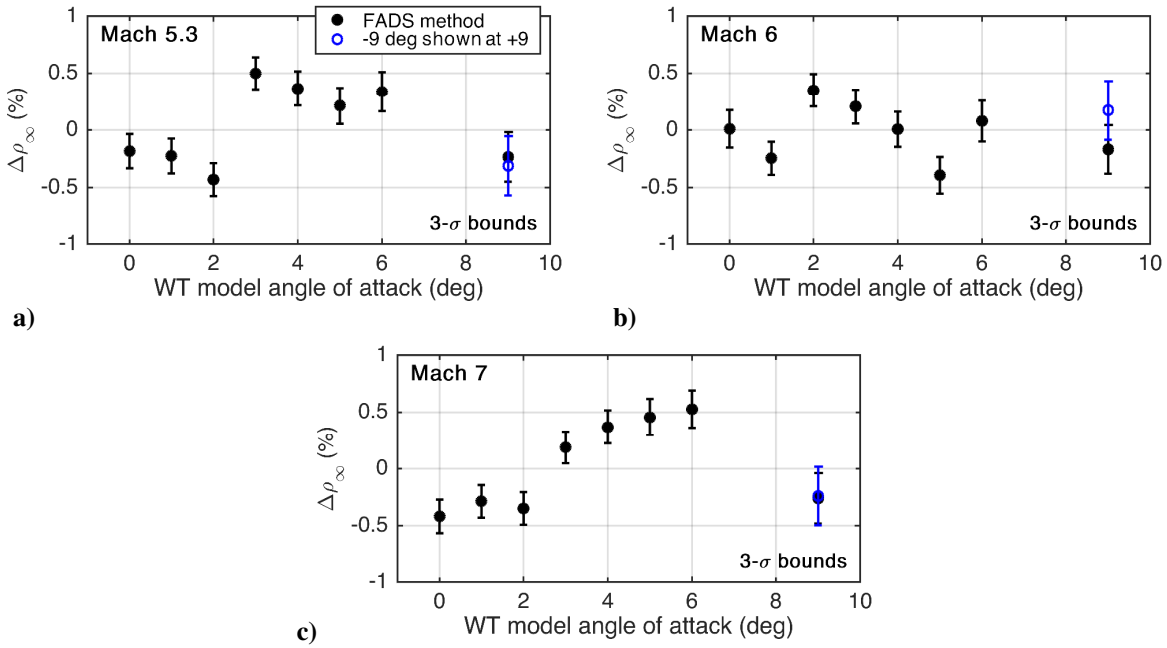

Fig. 8 FADS density w.r.t. average and Monte Carlo uncertainty (black), α –9° at +9° (blue).

The FADS density estimates in Fig. 8 are plotted as percentage deviations from the average reconstruction value, per Mach number. Their variations are within ±0.5% and scattered beyond the experimental uncertainties of ±0.15%. The latter are smaller than the ±0.5% errors imposed on pressure data in the Monte Carlo, because density influences the pressure distribution uniformly, allowing errors at individual ports to cancel out partially. Without an independent density measurement of similar accuracy, it is not possible to separate the 0.5% variations into wind tunnel uncertainty and FADS reconstruction error. As the flow angles are within experimental uncertainties, we do not expect the density variations to indicate an issue with the FADS method or CFD pressure model. [37] mentions that the wind tunnel Mach number uncertainty is ±0.05, which corresponds to stagnation pressure variations of 3 to 4% at Mach 7 and Mach 5.3. We did not consider the Mach number as an error source, however this would clearly expand the uncertainty bounds to contain the density scatter. If instead the CFD pressure model is the cause, it would suggest an error in the shock wave pressure ratio.

IV. FADS performance for simulated EDM entry

The method from Section II is applied to synthetic pressure data to quantify the FADS performance during entry. Uncertainty bounds on the reconstructed flow angles and atmospheric density are determined along a nominal EDM

trajectory using Monte Carlo analysis. Altitudes range from 60 km down to 9 km, i.e. the continuum flow regime between Mach 28.5 and 2. We use the CFD pressure model developed in [37] for the simulated EDM flight conditions. CFD uncertainties are based on [37], where the sensitivity of modeled pressures to various assumptions regarding chemistry, laminar flow, and atmospheric composition has been quantified. The CFD uncertainty is also based on the experiments in Section III, where the flow angle reconstruction performance in the wind tunnel is considered.

A. Simulated EDM trajectory

Synthetic FADS pressure data are generated as a function of Mach number, dynamic pressure, and flow angles given by an atmospheric entry simulation. We simulate nominal and off-nominal trajectories, the latter to provide an upper bound on the expected total angle of attack due to aerodynamic uncertainties.

Table 1 Nominal trajectory state at 120 km of the EDM.

geodetic altitude	120	km
geodetic latitude	4.7	deg
geodetic longitude	344.5	deg
angle of attack	0	deg
sideslip angle	0	deg
relative velocity	6000	m/s
flight path angle	–12.1	deg
heading East from North	124	deg

The simulator numerically integrates standard flight dynamics equations from [40] and [41] using a 4^{th} order Runge-Kutta method with constant 10 ms time step. Simulation inputs are the initial trajectory state, vehicle mass distribution, aerodynamic coefficients, and models of the gravity and atmosphere on Mars. The initial state is specified at 120 km and in Table 1, and identical in nominal and off-nominal simulations. The initial atmosphere relative velocity is 6.0 km/s with a flight path angle of –12.1° below the local spherical horizon. Geodetic coordinates[**] are relative to a planet-centered ellipsoid with equatorial and polar radius of 3396.19 km and 3376.20 km, respectively [42]. An ellipsoid gravity model is used, and the Mars rotation rate is $4.0612\ 10^{-3}$ °/s. Atmospheric conditions, i.e. density, pressure, temperature, and winds are extracted from the Mars Climate Database (MCD), using the climatology scenario [43]. The MCD wind profiles are shown in Fig. 9, they are averaged over time hence do not include wind gusts. The winds are westbound

[**] While 'geodetic' usually refers to Earth only, for Mars entry this term is also used in the literature, e.g. [33].

and roughly along the equatorial trajectory of the EDM. Since the winds are not reconstructed by FADS, the MCD wind predictions will be used in Section IV to investigate errors due to assuming zero winds. We assume a constant mass of 600 kg for the EDM until parachute deployment. The EDM is spin stabilized with an initial roll rate of 15 rpm approximately maintained during entry [11][12]. The mass distribution of the EDM is given in Table 2, where the CG location was determined from IMU flight data by industry. The radial CG offset is 7.2 mm and larger than the design value of 5.4 mm, increasing the trim angle.

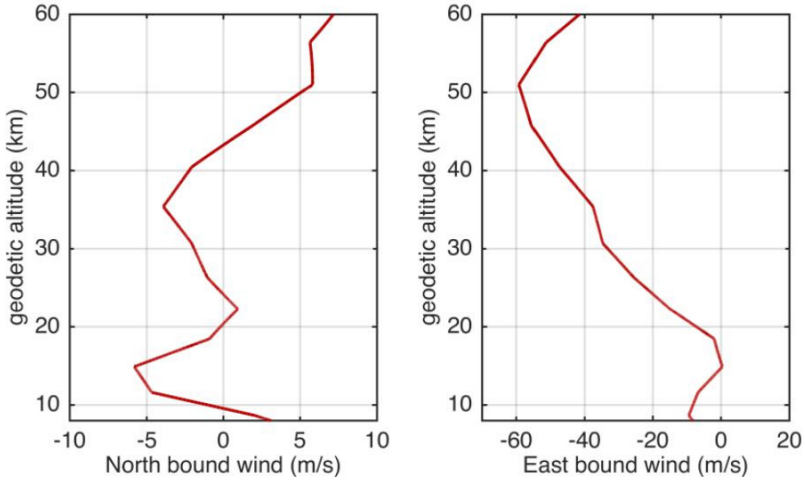

Fig. 9 Wind profiles from Mars Climate Database (MCD).

Because the EDM aeroshell geometry is nearly identical to that of the 2008 Phoenix mission, we use the aerodynamic force, static moment, and dynamic moment coefficients for Phoenix published in [21]. The aerodynamic coefficients are based on Navier-Stokes CFD solutions that consider equilibrium and NEQ chemistry, and additional data sources described in [21]. The applicability of the Phoenix aerodynamics for the EDM must be justified beyond the similar aeroshell geometry. Importantly, static moment instabilities were predicted for Phoenix and observed in flight. Referred to as bounded static instability, because this only occurs at low angles of attack, it was first predicted for Pathfinder [44] and is a consequence of NEQ chemistry displacing the sonic line and changing the pressure distribution. The instability might occur in two trajectory regions: the transitional regime above 6 km/s and the hypersonic regime near 3.5 km/s. Only the second instability is relevant here as we consider the continuum regime, and would occur near peak dynamic pressure where FADS pressure data are most accurate. The exact trajectory location of the instability, and whether it happens at all, depend on the specific density-velocity conditions. At corresponding velocities in the hypersonic regime, the EDM simulation has about 20% higher density than Phoenix. According to [21], such density variation does not influence the static instability much. However, the CG location of the EDM does have a crucial influence.

While Phoenix was designed to trim near $\alpha_T = 0°$, the large radial CG offset on the EDM produces a total angle of attack above 2° (see Fig. 11). This eliminates the importance of the bounded instability, which is limited to that range [21]. Consequently, the Phoenix database can be used to good approximation for the EDM, even if their trajectory conditions are not identical.

Table 2 Nominal mass distribution of the EDM.

center of gravity (CG)	**axial location**[††]	mm	–605
	radial y-offset	mm	-0.5
	radial z-offset	mm	7.2
moments of inertia (MOI)	**body x-axis**	$kg \cdot m^2$	254
	body y-axis	$kg \cdot m^2$	165
	body z-axis	$kg \cdot m^2$	180
	off-axis x-y	$kg \cdot m^2$	-3
	off-axis y-z	$kg \cdot m^2$	-1
	off-axis x-z	$kg \cdot m^2$	2

Atmosphere relative velocity and dynamic pressure along the simulated nominal trajectory are plotted in Fig. 10 against geodetic altitude in the continuum regime below 60 km. The velocity decreases more rapidly when dynamic pressure q_∞ is higher, since aerodynamic drag is proportional to q_∞. In turn, the forebody pressures measured by FADS are proportional to dynamic pressure. q_∞ reduces from its maximum of 6.5 kPa near Mach 18 to about 1 kPa at Mach 2 near parachute deployment. Mach numbers are marked by symbols on Fig. 10, where open symbols indicate trajectory points at which CFD solutions were obtained in [37]. The CFD trajectory points are more densely spaced in the supersonic regime, as the pressure distribution is more sensitive to Mach number in this region [39]. The filled symbols mark additional Mach numbers, however no CFD was performed at those conditions. The CFD flow simulations were performed below Mach 14, as the EDM did not transmit any flight data during the blackout phase ending near Mach 14.

[††] Measured from the aeroshell nose

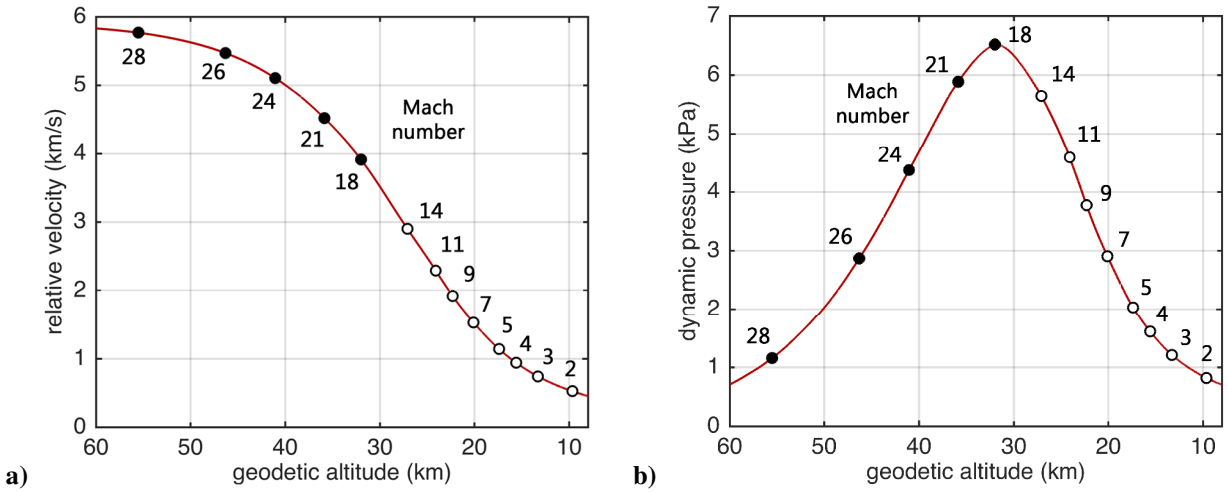

Fig. 10 a) Velocity and b) dynamic pressure on simulated EDM nominal trajectory, Mach numbers used in CFD (open symbols), and additional Mach numbers (closed symbols)

The off-nominal entry simulations have very similar velocity and dynamic pressure compared to nominal one, but significantly higher trim angles due to aerodynamic uncertainty. As the radial CG offset in the nominal case is already beyond the design value, it is not increased in the off-nominal case. We did confirm that an additional axial CG offset of 10 mm has negligible effect. Similarly, 5% perturbations of the MOI have no influence on the trim angle. Perturbations with respect to nominal aerodynamics are imposed based on the uncertainty bounds given in [21]. The values given here are 3-σ, while a simulation with 2-σ perturbations is included as well. Multiplier and adder perturbations of 20% and 0.002–0.005 are imposed on the static moment coefficient, which strongly influences the attitude behavior. The adder perturbations depend on Mach number, where the highest value is used in the supersonic regime below Mach 5, and the lowest value above Mach 10. Between these Mach numbers, the moment errors are interpolated linearly. Perturbations of ±0.15 on dynamic moment coefficients were considered but found to have negligible effect on trim angle. The axial force coefficient is increased by 3–10% with an analogous dependence on Mach number as for the static moment. Finally, the side force coefficient is increased by a constant value of 0.01 along the trajectory.

The angle of attack, sideslip angle, and total angle of attack are plotted in Fig. 11, black lines are the trim angle about which the EDM oscillates, calculated to produce zero torque in the CG. Results for the 2-σ case are omitted from the sideslip angle for clarity. The beat pattern is a consequence of the non-zero off-axis MOI (see Table 2). In all cases, the angle of attack is much larger than the sideslip angle, consistent with the CG offset in the pitch plane. In the off-nominal cases, the EDM trim angle is largest in the supersonic regime due to the moment uncertainty being high in that region. At about Mach 5, the total angle of attack reaches up to 8° (2-σ) and 11° (3-σ). The CFD

pressure model, described below, includes α_T values up to 10° which is sufficient to contain the expected EDM attitude in at least the 2-σ uncertainty range.

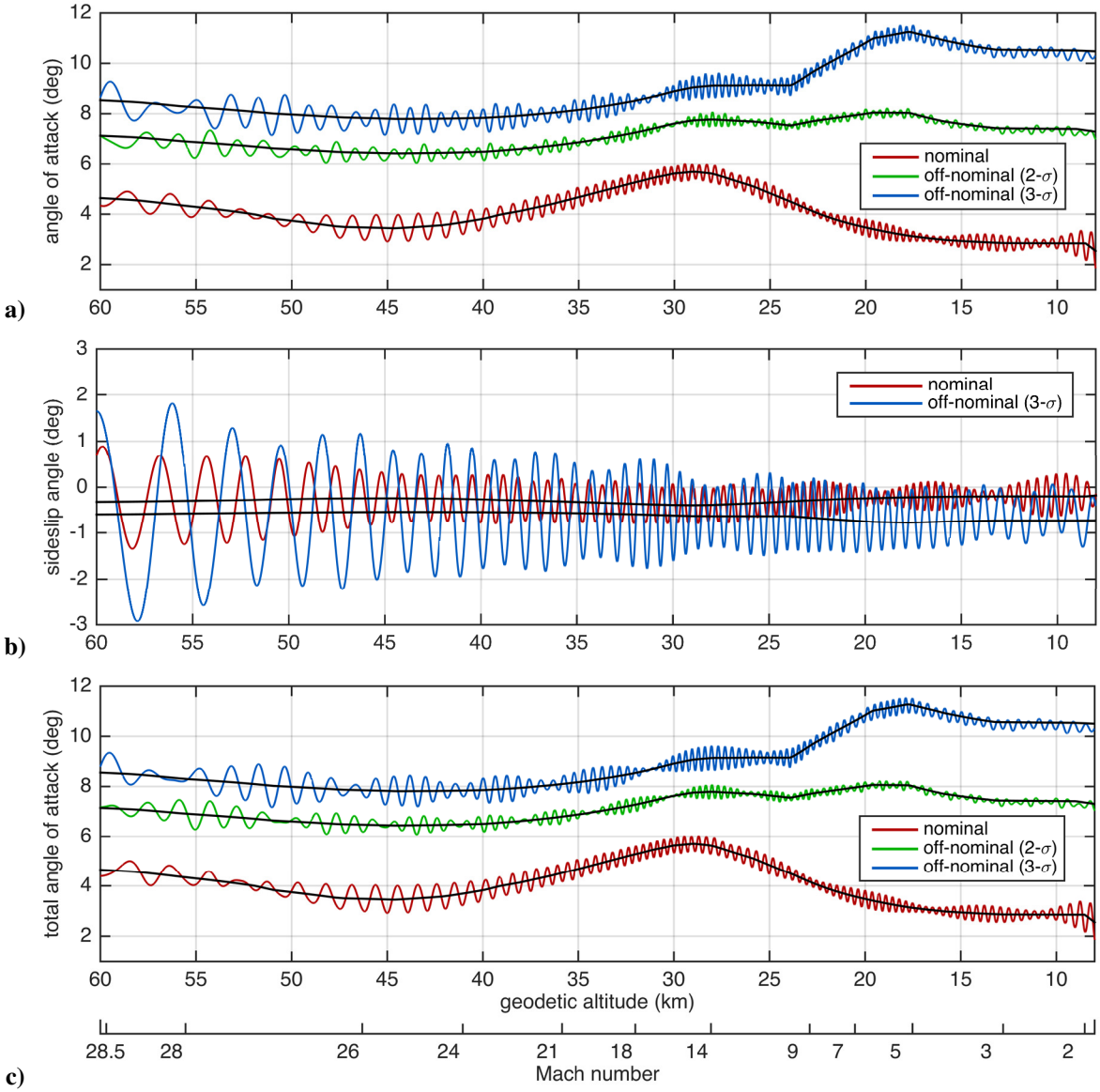

Fig. 11 Flow angles on nominal and off-nominal EDM trajectories, with trim angles (black).

B. CFD pressure model for flight

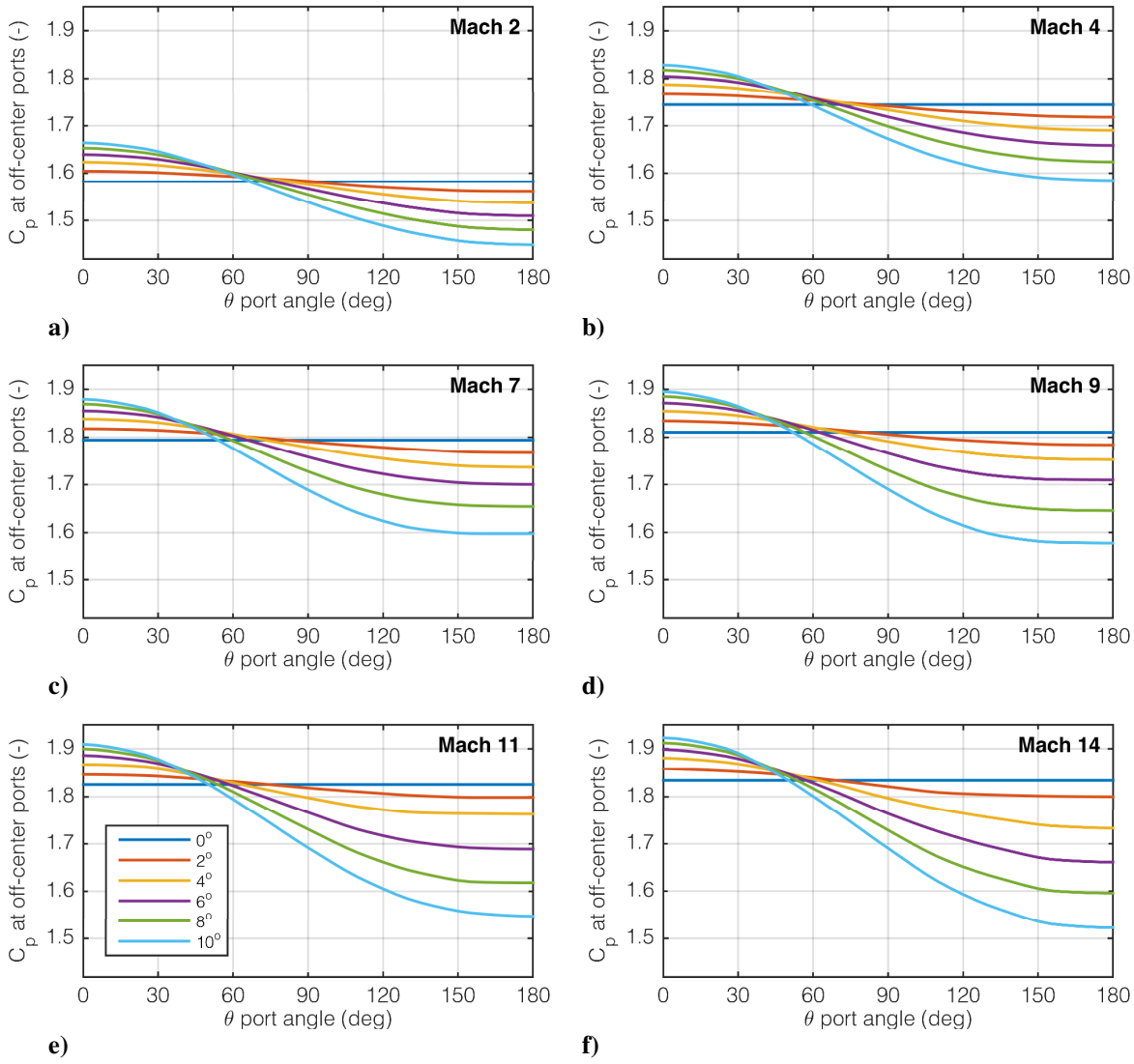

Fig. 12 CFD pressure model for EDM flight conditions, off-center pressure coefficients.

CFD modeling of the EDM pressure distribution was performed at Mach numbers of 2, 3, 4, 5, 7, 9, 11, and 14 shown in Fig. 11. The flow on the forebody of the EDM is laminar, therefore the viscous Euler equations were solved. In this paper, we assume the pressure distribution to be Mach independent above 14, i.e. we extrapolate the CFD to higher Mach numbers by assuming the pressure model constant. This approximation allows to extend the FADS analysis to the whole continuum flow regime, including peak dynamic pressure near Mach 18 or 30 km. It must be emphasized that the pressure distribution does change at higher Mach numbers, as seen for Pathfinder in [44], where predictions of the pressure distribution are given for Mach 9, 16, and 22. Our CFD pressure model reproduces the Pathfinder results at

Mach 9 and Mach 16 to within 1% (when the latter is compared to Mach 14). However, towards Mach 22 the pressure has changed again by up to 2% from Mach 16 results. Therefore, using the pressure model analyze actual flight data is not recommended, and we will impose uncertainty on the CFD pressure model to emphasize this point.

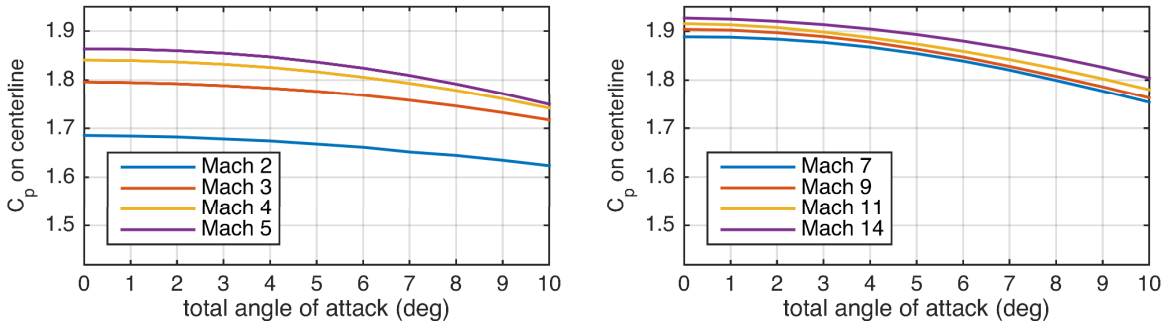

a) **b)**

Fig. 13 CFD pressure model for EDM flight conditions, centerline pressure coefficients.

The CFD pressure model is plotted in Fig. 12–Fig. 13 against total angle of attack and port angle θ at several Mach numbers. Surface pressures are given for total angles of attack ranging from 0° to 10° in 0.5° increments. Normalized pressure coefficients are extracted from CFD solutions on the EDM centerline, at port P0, and clocked along the radial distance of the off-center ports P1–P3 (see Fig. 1). The pressure distribution is less dependent on Mach number at hypersonic velocities above Mach 7, as expected. Pressure differences between windward and leeward side become smaller in the supersonic regime, which will have some consequences for FADS flow angle reconstruction. Other trends of the CFD pressure model are similar to those at wind tunnel conditions, described above in Section III.B.

CFD uncertainty affects the FADS reconstruction differently for density and flow angles. Because flow angles are sensitive to relative pressure differences, CFD errors that influence the whole pressure distribution are more important for density, i.e. the shock wave pressure ratio. Errors that influence the pressure variation across the forebody are more important for the flow angles. Table 3 gives the 3-σ uncertainties on the CFD pressure model used in the FADS flight study below. Firstly, 0.5% bias uncertainty is applied to the pressure distribution uniformly, representing errors on the shock wave pressure ratio. The uncertainty is high enough to account for the density scatter observed in the wind tunnel experiments, which could not be separated into CFD or experimental error (see Section III). Additional support for the 0.5% value was obtained by comparing the stagnation pressure of the CFD model to estimates from a 1-D normal shock solver. The latter is described in [35] and assumes thermochemical

equilibrium like the CFD, it has been used to reconstruct atmospheric profiles from MSL pressure data. Discrepancies between the 1-D solver and the CFD pressure model are less than 0.5% in hypersonic flight, and below Mach 5 reduce towards zero. Secondly, the CFD solutions above Mach 9 exhibited some wavy artefacts, which were carefully removed without changing the global pressure values in the model. The artefacts are caused by mesh discretization at the shock wave, leading to pressure waves that are damped out less when the shock is closer to the forebody at higher Mach numbers. Mesh uncertainty mainly affects the pressure distribution on the leeward side, downstream of the stagnation region. Regardless, the CFD mesh uncertainty in Table 3 is applied equally and independently at every off-center port location, to ensure that relative pressure differences across the forebody are perturbed to fullest extent. The mesh uncertainty is a function of Mach number and based on the maximum size of CFD corrections. These are 0.25%, 0.5% and 0.7% for Mach 9, 11, and 14, respectively. The corrections at Mach 9 were only 0.2%, but the uncertainty value was increased to lead to ±0.2° (3-σ) errors on α, β, the validation level obtained in the wind tunnel experiments. For the same reason, the mesh uncertainty is maintained at a constant 0.25% below Mach 9.

Table 3 CFD pressure model uncertainties (3-σ).

Mach number	bias	mesh	NEQ off-center	NEQ centerline
15+	0.5%	0.7%	2.0%	2.0%
14	0.5%	0.7%	0.8%	1.4%
11	0.5%	0.5%	0.2%	0.4%
9	0.5%	0.25%	0.1%	0.2%
7–	0.5%	0.25%	0.0%	0.0%

Thirdly, the CFD solutions make several assumptions that were investigated in [37]. Assuming laminar flow and the Mars atmospheric gas composition have negligible effect on the pressure distribution, no uncertainty is assigned for these. However, assuming chemical equilibrium above Mach 9 results in significant error at both centerline and off-center ports. To quantify the consequences of neglecting NEQ chemistry, additional CFD was performed in [37] at zero angle of attack (3-D computations for positive α_T were too time consuming). The NEQ uncertainty based on those solutions is negligible below Mach 9, but at Mach 14 reaches 1.4% on the centerline and 0.8% at off-center ports. Importantly, when the CFD pressure model is extrapolated above Mach 14, further variations in the gas chemistry are not considered. To account for this, the NEQ uncertainty is increased to 2% at Mach 15 and kept constant at higher Mach numbers. The 2% is based on the pressure variations between Mach 16 and Mach 22 predicted for Pathfinder in [44]. Early on in the trajectory, near 60 km, the atmosphere is very low density and the pressure distribution tends towards ideal gas behavior, referred to as

frozen flow. Differences between the equilibrium CFD and non-reacting ideal gas solutions are given in [37] and amount to 2% again, hence the NEQ uncertainties in Table 3 also contain the influence of neglecting frozen flow.

A final consideration is that the CFD pressure model is used along a simulated EDM trajectory that assumes an aerodynamic model based on different CFD solutions [21]. The aerodynamic coefficients depend on the integrated pressure distribution, mainly on the forebody in hypersonic flight. If the FADS reconstruction of density and flow angles is used to validate an aerodynamic database, it is preferable for the pressure model to be consistent with the aerodynamics model, at least near the pressure ports. This is less important in the current work, which requires only a representative trajectory and attitude behavior to analyze FADS performance on its own. Nevertheless, we derived aerodynamic coefficients from the CFD presented here. Below Mach 5, the coefficients are in excellent agreement with the aerodynamics model from [21]. The axial force and moment coefficients are within 0.2 standard deviations of the aerodynamic uncertainty, and the normal force is within 0.6. All coefficients agree within the 1-σ uncertainty below Mach 9, while at Mach 11 and 14 the moment differs by up to 2.6 and 1.7 standard deviations, respectively. At Mach 14 and below 2° total angle of attack, the axial force disagrees by up to 1.4 deviations. The reduced agreement at high Mach numbers is most likely due to neglecting non-equilibrium chemistry, already taken into account as a FADS uncertainty source in Table 3. When using the aerodynamics from CFD in the nominal EDM simulation, the trim angle changes by only 1° near Mach 11, and is unchanged below Mach 8.

C. Synthetic pressure data

Using the dynamic pressure and flow angles from the nominal EDM entry simulation, synthetic FADS pressure data were generated using the CFD pressure model just described. These are shown in Fig. 14 as physical pressures and normalized pressure coefficients. The EDM trims at positive angles of attack, so ports P2 and P3 are on the leeward side and measure the lowest pressures. Notice that the pressures at P2 and P3 are not the same, indicating that the EDM trims in a pitch plane that does not contain P1 exactly (see Fig. 1b) given the off-design CG location. Pressures at P2 are higher than at P3, because the former is closer to the stagnation point. Below about Mach 9, the pressure coefficients become smaller and approach each other in magnitude, especially at off-center port locations. The overall reduction is due to the decreasing Mach number in the supersonic regime, see Fig. 12, which weakens the shock and its pressure increase. Meanwhile, the total angle of attack also decreases (see Fig. 11c), reducing pressure differences across the forebody by making the distribution more axially symmetric.

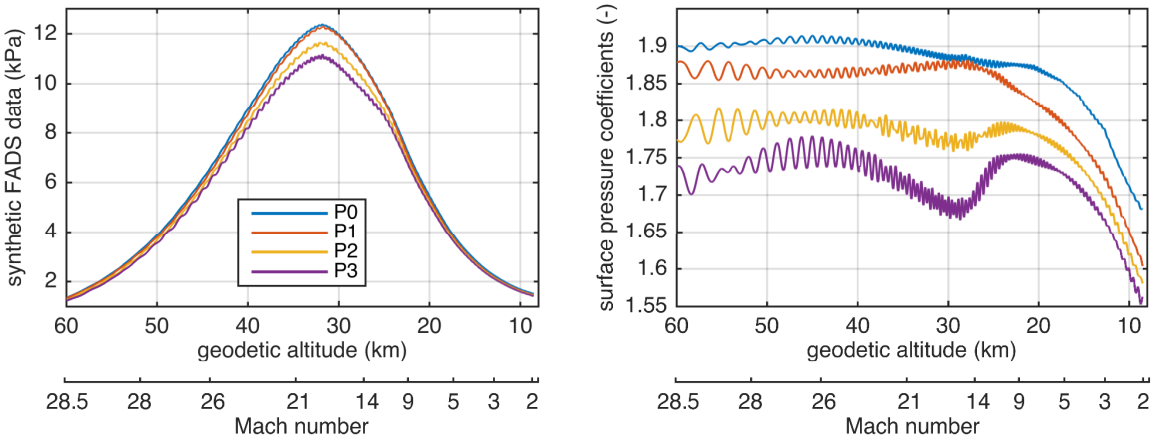

a) **b)**

Fig. 14 Synthetic FADS data for nominal trajectory a) in physical units and b) normalized.

To evaluate the sensitivity of FADS pressure ports to density and attitude, we generated synthetic data while imposing 0.1° deviations on α, β and 0.2% on density. Fig. 15 shows the resulting FADS sensitivities to angle of attack, sideslip angle, and atmospheric density. The sensitivities are different at every port, as they measure the pressure distribution at unique locations. Port P3 in Fig. 15a is most sensitive to angle of attack, due to its location on the leeward side farthest away from the stagnation region. The sensitivity is negative because larger α corresponds to lower leeward pressure. Port P2 in Fig. 15b is most sensitive to sideslip angle, as it is farthest from the aerodynamic trim plane. Large β correspond to low pressures at port P3, so again the sensitivity is negative. While P2 and P3 have the highest sensitivity to the flow angles, every off-center port provides information on attitude. Even port P0 on the vehicle centerline is influenced by α but least sensitive overall, as expected. Interestingly, the FADS sensitivity to attitude in Fig. 15a–b decreases rather strongly near 25 km or Mach 10, and continues to reduce in the supersonic regime. This is consistent with the increasing shock stand-off distance and reducing total angle of attack, as discussed for Fig. 14.

The FADS sensitivity to density is shown in Fig. 15c, where the centerline P0 and off-center P1 are slightly more sensitive, because the pressure at these ports is greatest. Port P1 measures high pressures due to the positive angle of attack, combined with the stagnation pressure region extending onto the conical part of the heat shield (see Fig. 1b). Although P2 and P3 measure slightly lower pressures, their sensitivities are very similar, because the atmospheric density has a global effect on the pressure distribution.

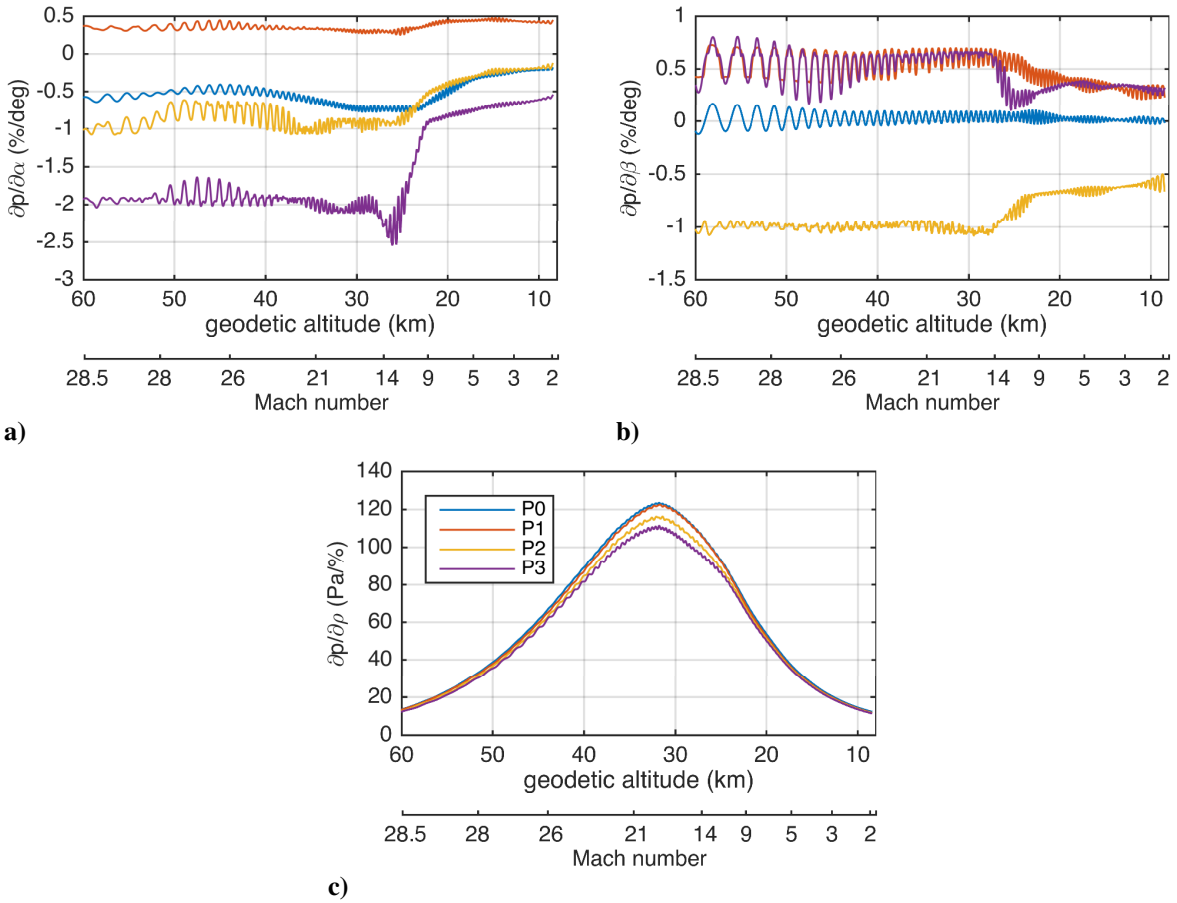

Fig. 15 Pressure sensitivity to a) angle of attack, b) sideslip angle, and c) atmospheric density.

D. Monte Carlo uncertainty analysis

We now quantify the FADS reconstruction uncertainty along the simulated EDM trajectory, between 60 km and 9 km, by processing the synthetic pressure data in a Monte Carlo of 1000 reconstructions. Gaussian errors are imposed on the flight data and CFD pressure model. The IMU relative velocity, which assumes zero winds, is perturbed with MCD wind profiles from Fig. 9, scaled by a zero mean normal distribution of ±1.2 (3-σ). The IMU altitude used in Eq. (2) is assumed to be known perfectly. Initial guesses for α, β, and ρ_∞ in the FADS solver (see Fig. 3) are taken from the FADS results at previous trajectory points, starting at 60 km with perfect values. The CFD pressure model uncertainty has been described in Section IV.B (see Table 3). CFD errors that depend on the Mach number are generated at one Mach value and then scaled consistently along the trajectory. CFD bias errors are applied uniformly to the pressure distribution, and errors at off-center port locations are generated independently for every port. This ensures that they influence the FADS flow angle reconstruction by influencing the relative pressure distribution.

The sensor uncertainties are modeled as a combination of sensitivity and bias error. While the bias can be eliminated before entry, in the vacuum of space, a residual bias error will accumulate during flight due to temperature effects and hysteresis. Calibration of the EDM pressure sensors by industry provides some information on residual bias, involving one thermal cycle in which pressure calibrations were carried out at 23, -50, 140, and 23°C. The results suggest a temperature dependence of the bias of –3 Pa/°C. We combined this value with temperature increases from the actual flight, measured on the back of the heat shield [12]. The temperature increases are 4 and 8 °C at off-center and centerline ports respectively, resulting in bias errors of at most 24 Pa near parachute deployment. This corresponds to 0.10% on the full scale range of 25 kPa. We increased the value to 0.15% to account for hysteresis, which was not investigated in the calibration. In the Monte Carlo analysis, the maximum bias error at every port is randomly distributed as ±0.15% (3-σ) and increases linearly from zero at the initial entry state. The bias can then reach ~40 Pa, which is comparable to the largest bias error of 47 Pa observed in the post-flight analysis of MSL [9]. It should be mentioned that the FADS instrumentation on MSL generally performed much better, with other biases being on the order of 5 Pa. However it was also calibrated more rigorously, e.g. by accurately determining the temperature dependency of pressure errors [13]. The sensitivity uncertainty for the EDM is assumed as 0.6% (3-σ) which is the mean sensitivity change in the calibration before and after thermal cycling, at 23°C. The largest variation was 1% while fitting a temperature dependence as done for bias predicts variations of only 0.2%, the value of 0.6% lies between these possibilities.

Monte Carlo uncertainties on the FADS reconstruction are plotted against geodetic altitude and Mach number in Fig. 16. Uncertainty due to the pressure sensors, CFD model, assuming zero winds, and the combined effect are included. The combined uncertainty on the flow angles is largest below Mach 5, reaching 4° at Mach 2 due to accumulated sensor bias and the low dynamic pressure. By comparison, the density reconstruction is affected much less because the bias errors are uncorrelated between the ports and tend to cancel out. Nevertheless, the uncertainty on density reaches 5% due to ignoring winds: as the EDM velocity reduces the winds have more impact on IMU velocity. In fact, they result in significant density uncertainty during most of the entry, as they are mainly directed along the EDM trajectory (equatorial) and increase with altitude (see Fig. 9). By contrast, the flow angle uncertainty is independent of the winds. Regarding the CFD modeling uncertainty, there is a clear distinction between the trajectory above and below the Mach 14 region. At higher altitudes, the assumption of equilibrium flow and extrapolation of the CFD model are penalized with large uncertainties (see Table 3), exceeding those of the sensors. In this trajectory range, the combined uncertainty on the flow angles is almost constant at 1° and about 3% on density. In the lower trajectory range, the CFD is most accurate and below the sensor uncertainty, even for the density.

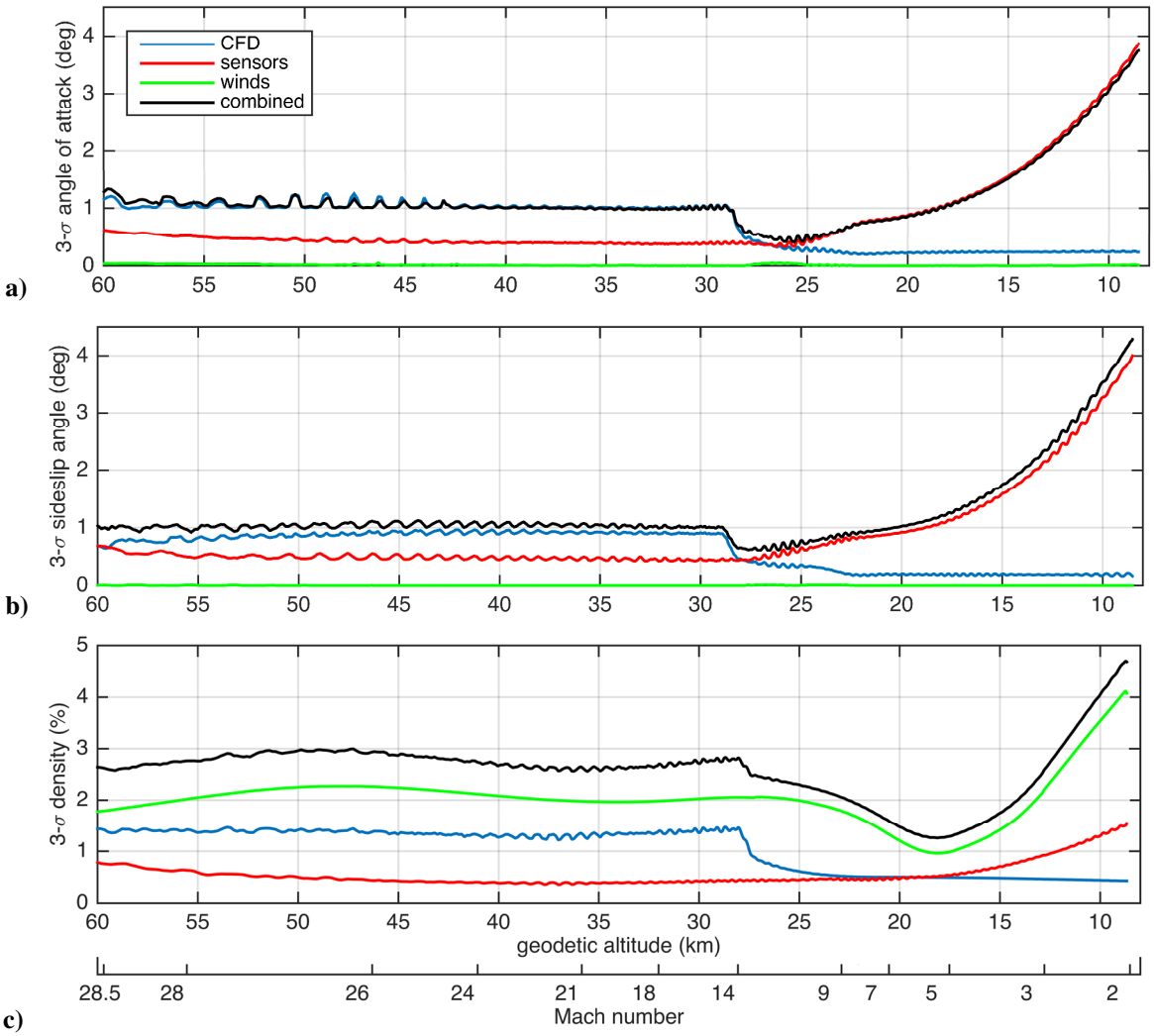

Fig. 16 FADS uncertainty on nominal EDM trajectory, due to CFD pressure model (blue), pressure data (red), assuming zero winds (green), and combined uncertainty (black).

Atmospheric pressure, temperature, and Mach number as derived with Eq. (1–3) from reconstructed density (see Fig. 3) are shown in Fig. 17. The molecular weight and heat capacity ratio were given by MCD as function of altitude and assumed perfectly known. At 60 km, the hydrostatic boundary condition in Eq. (2) was assigned 5% uncertainty (3-σ). This uncertainty dominates the atmospheric reconstruction down to about 50 km and vanishes at lower altitudes, because p_∞ increases exponentially towards the ground. Below 50 km, the p_∞ uncertainty is similar to that on density in Fig. 16c, but influenced less by winds at low altitudes, reaching about 2.5%. As opposed to other relations used in the FADS method, the hydrostatic pressure integration depends on previous trajectory points and is able to propagate errors along the trajectory. The consequences of this are seen by comparing the contributions of CFD uncertainty on atmospheric density and pressure. After the density uncertainty has decreased rapidly below Mach 14, the large initial uncertainty

is propagated to lower altitudes by the pressure integration while decaying. This is the typical response of integrators to a step signal. When p_∞ and ρ_∞ are divided through each other in the ideal gas law to reconstruct temperature, only common errors are able to cancel out, so the different uncertainties on p_∞ and ρ_∞ lead to an abrupt increase of the temperature uncertainty. A similar phenomenon occurs for the wind errors, which depend on altitude and have a complex effect on the temperature, even reducing to zero near 15 km. Finally, the Mach number uncertainty is driven by the pressure boundary condition above 50 km, and at lower altitudes by assuming zero winds.

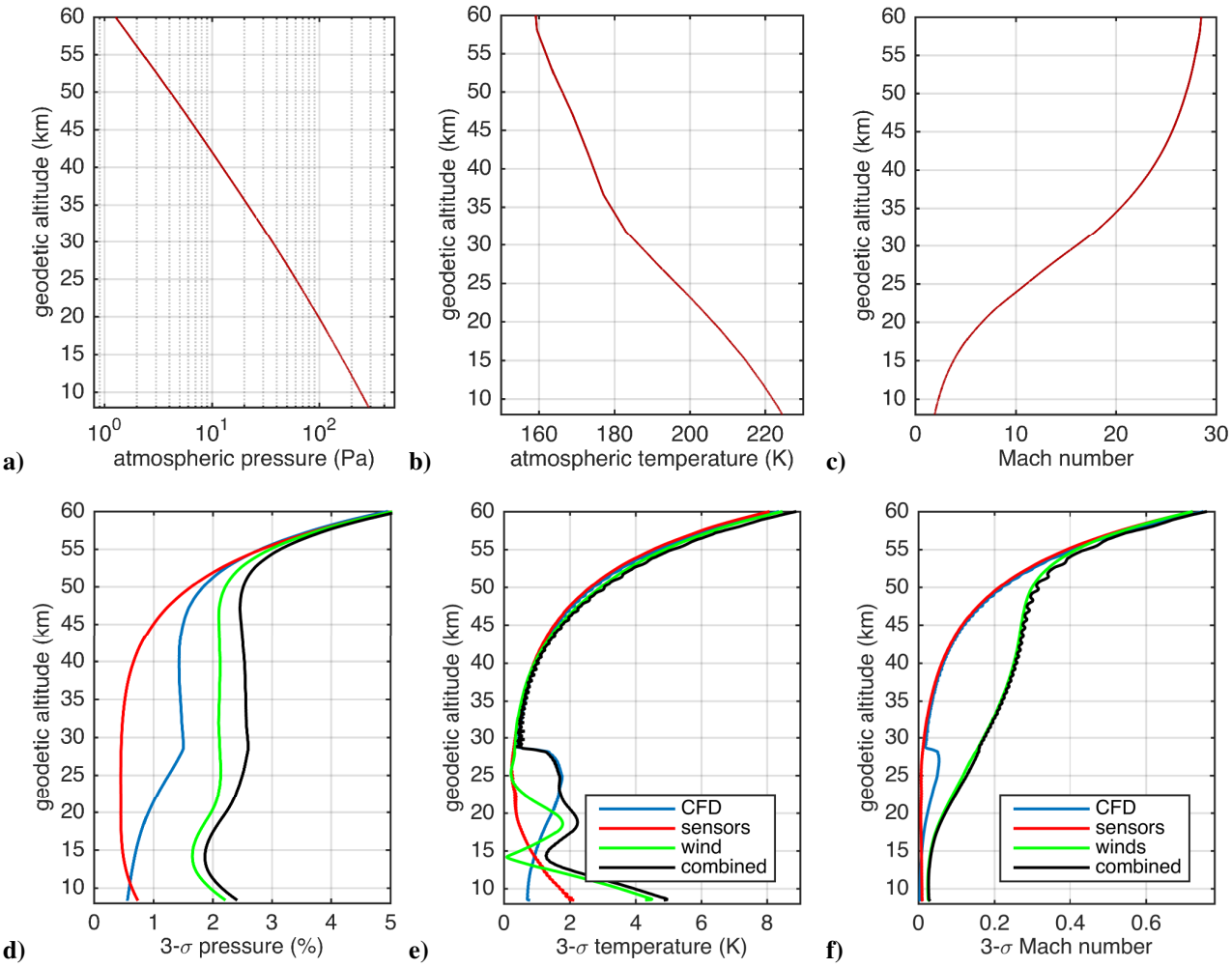

Fig. 17 FADS uncertainty on nominal EDM trajectory, due to CFD pressure model (blue), pressure data (red), assuming zero winds (green), and combined uncertainty (black).

E. Discussion

Our results show that FADS performance for the EDM varies significantly along the trajectory. This is mainly the result of changes in the CFD uncertainty and the accumulation of residual bias on the pressure data. In the hypersonic regime above Mach 14 the CFD model is the main source of uncertainty, see Fig. 16, because it was

developed for lower Mach numbers and extrapolated to above 30 km. For the flow angles in the supersonic regime, residual bias errors essentially prohibit an accurate reconstruction below about Mach 3. This is seen in Fig. 18a–b, where the attitude behavior of the EDM can be resolved as long as the uncertainty bounds are modest compared to the trim angle. Above Mach 7, corresponding to about 20 km, the FADS reconstructs the flow angles to within 1° (3-σ), which is sufficient to resolve attitude. The average residuals on reconstructed flow angles in the Monte Carlo analysis are shown in Fig. 18c, to demonstrate they are negligible even when the uncertainty bounds are large.

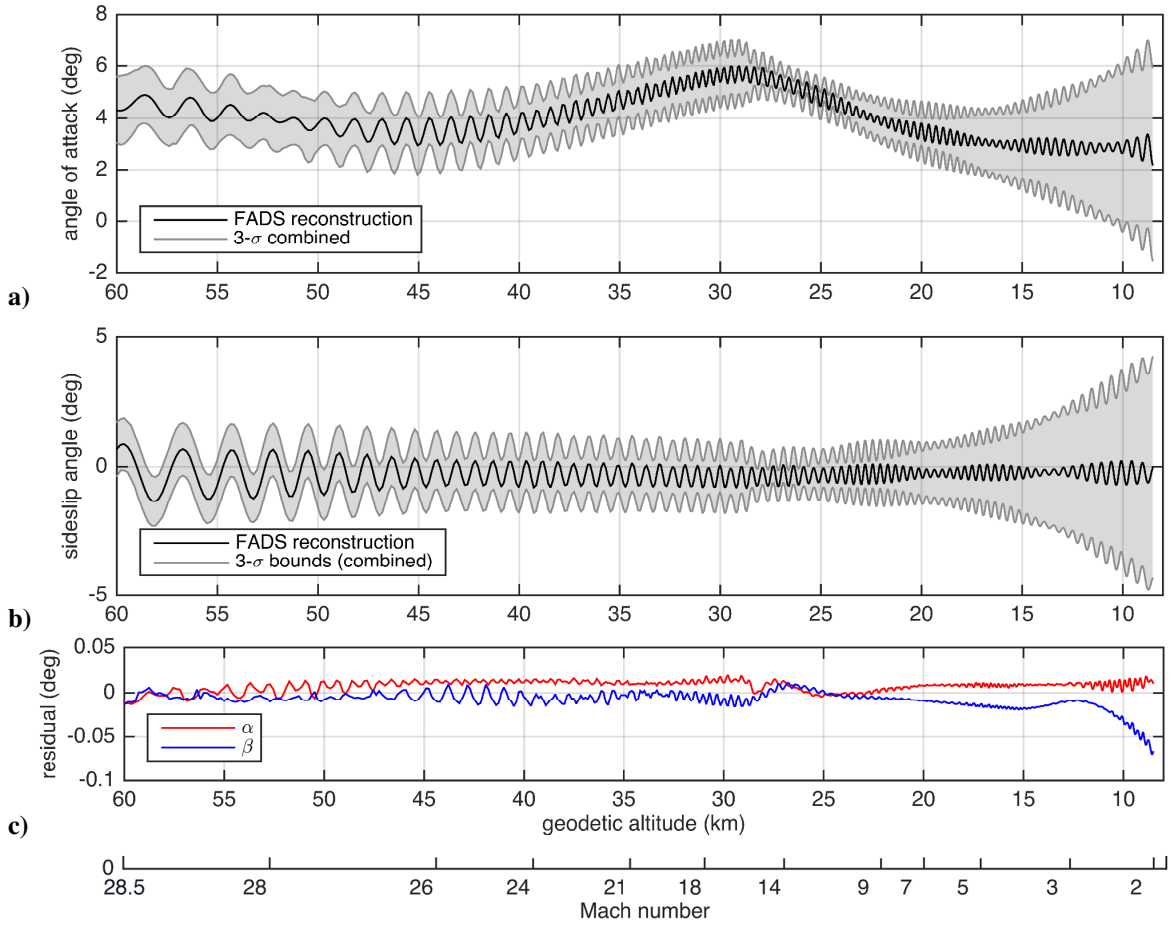

Fig. 18 FADS uncertainty on a) angle of attack, b) sideslip angle, c) Monte Carlo residuals.

A less prominent feature of the flow angle uncertainties in Fig. 16a–b, is that they are not identical for the angle of attack and sideslip angle. Minimum uncertainties of 0.4° (3-σ) are reached for α compared to 0.6° for β. The influence of CFD and sensor uncertainties differs slightly along the trajectory, which is a consequence of having only four pressure ports on the EDM, combined with their sensitivity to flow angles depending on their forebody location (see Section IV.C). In other words, the flow angle uncertainty becomes dependent on the attitude itself. In

the present case of large CFD uncertainties above Mach 14, or large measurement errors below that, this aspect is of secondary importance. However if these uncertainties were reduced, it is likely that a greater number of FADS ports would be required to reach the performance of e.g. MSL, which achieved 0.3–0.5° (3-σ) for both flow angles [13]. Indeed, the wind tunnel experiments in Section III demonstrated consistent accuracy of ±0.2° using 9 pressure ports, given low CFD and pressure data uncertainties.

Assuming zero winds has negligible effect on the reconstructed flow angles, but this also means that the latter contain little information for wind estimation by combination with IMU data, as done for MSL [9]. On the other hand, the atmospheric reconstruction is strongly affected by the winds along the entire trajectory. It should be noted that missing wind information is not specific to the FADS method, but plays the same role in atmospheric reconstructions based on IMU flight data. When both FADS and IMU data are available, the value of a FADS can be judged by its ability to reconstruct density more accurately than the uncertainty on aerodynamic forces, which affect IMU reconstructions. Above Mach 10 the FADS reconstruction is about as accurate as the 3% uncertainty on the axial force coefficient. The aerodynamics uncertainty increases to 10% below Mach 5, while that on the FADS stays under 5%. This means that the FADS on the EDM is sufficient to confirm other atmospheric reconstructions, but not likely to offer improved accuracy. In the hypersonic regime this is not only due to the winds, but also because the pressure model does not include NEQ chemistry. Heat shield ablation and deformation were also not neglected, as we have no such information for the EDM. The chemistry affects overall FADS performance, while ablation should be most important for the flow angle reconstruction.

V. Conclusion

We presented a method to estimate the attitude and atmospheric conditions from forebody surface pressures measured during entry, using a Flush Air Data System. The angle of attack, sideslip angle, atmospheric density, pressure, temperature, and Mach number are reconstructed by combining the pressure data with a CFD pressure model. The FADS method also requires the relative velocity and altitude, here provided by IMU. We studied the performance of the method in a hypersonic wind tunnel and along a simulated ExoMars EDM trajectory. The wind tunnel experiments were used to validate the CFD pressure model and methodology, by reconstructing the flow angles and density. The flow angles are in excellent agreement of ±0.2° with reference values from the wind tunnel sting mechanism. While much attention was paid to reduce experimental uncertainty, see the companion paper [37],

it is still possible for the CFD pressure model to be more accurate than could be proven experimentally. The density reconstruction was only validated qualitatively, but showed no unusual behavior.

In the EDM flight study, the FADS performance is adequate at least above Mach 5, with flow angle uncertainties of about 1° (3-σ) and density uncertainties of 1–3%. In the hypersonic regime above Mach 14, about half of the total uncertainty is due to assuming equilibrium chemistry in the CFD pressure model, which could be resolved with additional CFD computations. However, this is not much of an issue for the EDM post-flight analysis, as no flight data were retrieved during the blackout period above Mach 14. In the supersonic regime, bias errors on the pressure data result in large uncertainty on the flow angles starting near Mach 10, and become problematic below Mach 3 where they reach 4°. This underlines the importance of sensor calibration, which for the EDM is less accurate than the state of the art. The impact of biases and other errors can also be reduced by installing more FADS pressure ports (as was demonstrated in the wind tunnel experiments). Some unexpected features were found in the FADS uncertainty analysis, i.e. the increase of temperature errors due to the delayed response of atmospheric pressure to changing density errors, and the dependence of flow angle errors on the wind-relative attitude itself. Given the magnitude of other errors however, these are of secondary importance for the EDM.

Overall, the FADS instrumentation is useful to constrain both the flow angles and atmospheric conditions along the trajectory. The main difficulty for flow angles reconstruction are pressure bias errors in the supersonic regime. The main challenge for atmospheric reconstruction is the consequence of assuming zero winds. As the EDM trajectory is aligned with the dominant wind direction, the relative velocity from IMU is the primary error source for atmospheric density, pressure, and temperature. In post-flight analysis, it may be worthwhile to assume wind profiles from an atmospheric model.

Acknowledgements

This study was supported by the Belgian Science Policy Organization (BELSPO) and received funding from the European Union's Horizon 2020 Program (H2020-Compet-08-2014) under grant agreement UPWARDS-633127. The authors are grateful to the ExoMars Schiaparelli team for their support and discussions, in particular Olivier Bayle, Andrew Ball, and Leila Lorenzoni (ESA), Stefano Portigliotti (TAS-I), and Davide Bonetti (Deimos Space). We also thank our colleagues in the AMELIA science team, which is responsible for the EDM atmospheric reconstruction, including Francesca Ferri, Alessio Aboudan, and Giacomo Colombatti. We appreciate our

anonymous reviewers for providing insightful comments and suggesting relevant literature, which contributed significantly to the quality of this paper.

References

[1] Harvey, B., 2007 "The Mars 6 Landing," 12th March 1974 Journal of the British Interplanetary Society, Vol. 60, pp. 109–117.

[2] Harvey, B., "Russian Planetary Exploration: History, Development, Legacy and Prospects," Springer Praxis Books, ISBN 978-0-387-46343-8. Praxis Publishing Ltd, Chichester, U., doi: 10.1007/978-0-387-49664-1

[3] Euler, E. A., Adams, G. L., and Hopper, F. W., "Design and Reconstruction of the Viking Lander Descent Trajectories," *Journal of Guidance and Control*, Vol. 1, No. 5, 1978, pp. 372–378, doi:10.2514/3.55795

[4] Ingoldby, R. N., Michel, F. C., Flaherty, T. M., Doty, M. G., Preston, B., Villyard, K. W., and Steele, R. D., "Entry Data Analysis for Viking Landers," Contract report, NASA CR-159388, 1976.

[5] Cooley, C. G., "Viking 75 project: Viking lander system primary mission performance report," Technical report, NASA TN D-4185, 1977.

[6] Spencer, D. A., Blanchard, R. C., Braun, R. D., Kallameyn, P. H., and Thurman, S. W., "Mars Pathfinder Entry, Descent, and Landing Reconstruction," *Journal of Spacecraft and Rockets*, Vol. 36, No. 3, 1999, pp. 357–366, doi:10.2514/2.3478.

[7] Blanchard, R. C., and Desai, P. N., "Mars Phoenix Entry, Descent, and Landing Trajectory and Atmosphere Reconstruction," *Journal of Spacecraft and Rockets*, Vol. 48, No. 5, 2011, pp. 809–821, doi:10.2514/1.46274.

[8] Braun, R. D., and Manning, R. M., "Mars Exploration Entry, Descent, and Landing Challenges," *Journal of Spacecraft and Rockets*, Vol. 44, No. 2, 2007, pp. 310–323, doi: 10.2514/1.25116.

[9] Karlgaard, C. D., Kutty, P., Schoenenberger, M., Munk, M., Little, A., Kuhl, and C. A., Shidner, J., "Mars Science Laboratory Entry Atmospheric Data System Trajectory and Atmosphere Reconstruction," *Journal of Spacecraft and Rockets*, Vol. 51, No. 4, 2014, pp. 1029–1047, doi: 10.2514/1.A32770.

[10] Lorenzoni, L. V., "ExoMars 2016 Entry Descent and Landing Overview," *10th International Planetary Probe Workshop*, San Jose, CA, 2013.

[11] Bayle, O., Lorenzoni, L., Blancquaert, T., Langlois, S., Walloschek, T., Portigliotti, S., Capuano, M., "ExoMars Entry Descent and Landing Demonstrator Mission and Design Overview," *8th International Planetary Probe Workshop*, Portsmouth, VA, 2011.

[12] Portigliotti, S., Cassi, C., Montagna, M., Martella, P., Faletra, M., Boi, J., De Sanctis, S., Granà, D., Bayle, O., Blancquaert, T., and Lorenzoni, L., "EXOMARS 2016, the Schiaparelli Mission. EDL Demonstration Results from Real Time Telemetry before Unfortunate Impact," *14th International Planetary Probe Workshop*, The Hague, Netherlands, 2017.

[13] Karlgaard, C. D., Van Norman, J., and Siemers, P. M., "Mars Entry Atmospheric Data System Modeling, Calibration, and Error Analysis," Tech. Report, NASA TM-2014-218535.

[14] Van Hove, B., and Karatekin, Ö, "ExoMars 2016: attitude during Entry Phase", *14th International Planetary Probe Workshop*, The Hague, Netherlands, 2017.

[15] Swanson, et al., 2017, "MEDLI2 Do No Harm Test Series," *14th International Planetary Probe Workshop*, The Hague, Netherlands, 2017.

[16] Dyakonov, A. A., Schoenenberger, M., Van Norman, J. W., "Hypersonic and Supersonic Static Aerodynamics of Mars Science Laboratory Entry Vehicle," *30th AIAA Applied Aerodynamics Meeting*, New Orleans, LA, 2012, doi: 10.2514/6.2012-2999

[17] Edquist, K. T., Berry S., Kleb, B., Korzun, A., Dyakonov, A. A., Zarchi, K., Schauerhamer, G., Post, E., "Supersonic Retropropulsion Technology Development in NASA's Entry, Descent, and Landing Project," *9th International Planetary Probe Workshop*, Toulouse, France, 2012.

[18] Wright, M. J., Beck, R. A. S., Edquist, K. T., Driver, D., Sepka, S. A., Slimko, E. M., and Willcockson, W. H., "Sizing and Margins Assessment of Mars Science Laboratory Aeroshell Thermal Protection System," *Journal of Spacecraft and Rockets*, Vol. 51, No. 4, 2014, pp. 1125–1138, doi: 10.2514/1.A32579.

[19] Rohrschneider, R. R., Masciarelli, J., Miller, K. L., "A Comparison of Inflatable and Semi-Rigid Deployable Aerodynamic Decelerators for Future Aerocapture and Entry Missions," *8th International Planetary Probe Workshop*, Portsmouth, VA, 2011.

[20] Seiff, A., Reese, D. E., Jr., "Use of Entry Vehicle Responses to Define the Properties of the Mars Atmosphere," *Advances in the Astronautical Sciences*, Vol. 19, 1965, pp.419-447.

[21] Edquist, K. T., Desai, P. N., and Schoenenberger, M., "Aerodynamics for Mars Phoenix Entry Capsule," *Journal of Spacecraft and Rockets*, Vol. 48, No. 5 (2011), pp. 713-726, doi: 10.2514/1.46219

[22] Schofield, J. T., Barnes, J. R., Crisp, D., Haberle, R. M., Larsen, S., Magalhães, J. A., Murphy, J. R., Seiff, A., and Wilson, G., "The Mars Pathfinder Atmospheric Structure Investigation/Meteorology (ASI/MET) Experiment," *Science*, Vol. 278, No. 5344, 1997, pp. 1752–1758, doi: 10.1126/science.278.5344.1752.

[23] Clancy, R. T., and Sandor, B. J., "CO_2 ice clouds in the upper atmosphere of Mars," *Geophysical Research Letters*, Vol. 25, No. 4, 1998, pp. 489–492, doi: 10.1029/98GL00114.

[24] Withers, P., and Catling, D. C., "Observations of atmospheric tides on Mars at the season and latitude of the Phoenix atmospheric entry", *Geophysical Research Letters*, Vol. 37, No. 24, 2010, L24204, doi: 10.1029/2010GL045382.

[25] Withers, P., Catling, D. C., and Murphy, J. R., "Phoenix Entry Trajectory and Atmospheric Properties Reduced Data Records, PHX-M-ASE-5-EDL-RDR-V1.0", NASA Planetary Data System, 2010.

[26] Withers, P., and Smith, M. D., "Atmospheric Entry Profiles from the Mars Exploration Rovers Spirit and Opportunity," *Icarus*, Vol. 185, No. 1, 2006, pp. 133–142, doi:10.1016/j.icarus.2006.06.013.

[27] Holstein-Rathlou, C., Withers, P., and Maue, A., "Atmospheric Science from the Mars Science Laboratory Entry Probe," *12th International Planetary Probe Workshop*, Cologne, Germany, 2015.

[28] Withers, P., Towner, M. C., Hathi, B., and Zarnecki, J. C., "Analysis of Entry Accelerometer Data: A Case Study of Mars Pathfinder," *Planetary and Space Science*, Vol. 51, Nos. 9–10, 2003, pp. 541–561, doi:10.1016/S0032-0633(03)00077-1

[29] Smith, M. D., "Spacecraft Observations of the Martian Atmosphere", Annual Review of Earth and Planetary Sciences, Vol. 36, pp. 191-219, 2008, doi: 0.1146/annurev.earth.36.031207.12433.

[30] Wells, G. A., "A Comparison of Multiple Techniques for the Reconstruction of Entry, Descent, and Landing Trajectories and Atmospheres," Ph.D. dissertation, Daniel Guggenheim School of Aerospace Engineering, Georgia Institute of Technology, Atlanta, GA, 2011.

[31] Schoenenberger, M., Van Norman, J., Karlgaard, C., Kutty, P., and Way, D., "Assessment of the Reconstructed Aerodynamics of the Mars Science Laboratory Entry Vehicle," *Journal of Spacecraft and Rockets*, Vol. 51, No. 4, 2014, pp. 1076–1093 doi: 10.2514/1.A32794.

[32] Karlgaard, C. D., Kutty, P., Schoenenberger, M., Shidner, J., and Munk, M., "Mars Entry Atmospheric Data System Trajectory Reconstruction Methods and Flight Results," AIAA 2013-0028, *AIAA Aerospace Sciences Meeting*, Grapevine, TX, 2013, doi: 10.2514/6.2013-28.

[33] Chen, A., Cianciolo, A., Vasavada, A. R., Karlgaard, C. D., Barnes J., Cantor, B., Kass, D., Rafkin, S., and Tyler, D., "Reconstruction of Atmospheric Properties from Mars Science Laboratory Entry, Descent, and Landing," *Journal of Spacecraft and Rockets*, Vol. 51, No. 4, 2014, pp. 1062–1075, doi: 10.2514/1.A32708.

[34] Dutta, S., "Statistical methods for Reconstruction of Entry, Descent, and Landing Performance with Application to Vehicle Design," Ph.D. Dissertation, Daniel Guggenheim School of Aerospace Engineering, Georgia Institute of Technology, Atlanta, GA, 2013.

[35] Van Hove, B., Karatekin, Ö, "Atmospheric Reconstruction with Stagnation Pressure Flight Data from Mars Science Laboratory," *Journal of Spacecraft and Rockets*, Vol. 54, No. 3, pp. 609–620, doi: 10.2514/1.A33627.

[36] Golombek, M., et al., "Selection of the InSight Landing Site Space Science Reviews," 2017, doi: 10.1007/s11214-016-0321-9.

[37] Schleutker, T., Gülhan, A., Van Hove, B., Karatekin, Ö, "ExoMars Flush Air Data System: Experimental and Numerical Investigation", *Journal of Spacecraft and Rockets*.

[38] NASA Ames Research Staff, "Equations, Tables, and Charts for Compressible Flow," Tech. report, NASA TR-1135, 1953.

[39] Anderson, J. D., "Fundamentals of Aerodynamics," Tata McGraw-Hill Education, 2011.

[40] Stengel, R. F., “Flight Dynamics,” Princeton University Press, ISBN 978-0691114071, 2017.

[41] Cruz, J. R., “Flight Mechanics,” NASA Langley Research Center, http://bigidea.nianet.org/wp-content/uploads/2015/10/Flight-Mechanics-Lecture-Notes-V6.pdf, consulted on 9 October 2017.

[42] Seidelmann, P. K., Archinal, B. A., A'Hearn, M. F., Conrad, A., Consolmagno, G. J., Hestroffer, D., Hilton, J. L., Krasinsky, G. A., Neumann, G., Oberst, J., Stooke, P., Tedesco, E. F., Tholen, D. J., Thomas, P. C., Williams, I. P., “Report of the IAU/IAG Working Group on cartographic coordinates and rotational elements: 2006,” Celestial Mechanics and Dynamical Astronomy, Vo. 98, Iss. 3, pp.155-180, 2007, doi: 10.1007/s10569-007-9072-y.

[43] Millour, E., et al., “The Mars Climate Database (MCD version 5.2)”, *EPSC Abstracts*, Vol. 10, EPSC2015-438, 2015.

[44] Gnoffo, P. A., et al., “Prediction and Validation of Mars Pathfinder Hypersonic Aerodynamic Database”, Journal of Spacecraft and Rockets, Vol. 36, No. 3, 1999, pp. 367–373, doi: 10.2514/2.3455.